

28

Reliability Assessment of Aircraft Structure Joints under Corrosion- Fatigue Damage

28.1	Introduction	28-1
28.2	Current Engineering Philosophy	28-2
	Deterministic Approach • Risk-Based Approach	
28.3	Corrosion-Fatigue-Damage Modeling.....	28-8
	Fatigue Damage • Corrosion Damage • Corrosion-Fatigue Damage	
28.4	Reliability of Aircraft Structure Joints Including Maintenance Activities.....	28-35
	Risk/Reliability-Based Condition Assessment	
28.5	Illustrative Examples	28-39
	Probabilistic Life Prediction Using Different Corrosion-Fatigue Models • Risk-Based Maintenance Analysis of a Lap Joint Subjected to Pitting Corrosion and Fatigue	
28.6	Concluding Remarks.....	28-55

Dan M. Ghiocel

Ghiocel Predictive Technologies Inc.

Eric J. Tuegel

Air Force Research Laboratory

28.1 Introduction

A continuing challenge in the aviation industry is how to keep aircraft safely in service longer with limited maintenance budgets. Probabilistic methods provide tools to better assess the impact of uncertainties on component life and risk of failure. Application of probabilistic tools to risk-based condition assessment and life prediction helps managers to make better risk-informed decisions regarding aircraft fleet operation and airworthiness. In addition to assessing aircraft reliability, probabilistic methods also provide information for performing an analysis of the cost of continuing operation based on risks and their financial consequence.

Corrosion and fatigue, separately or in combination, are serious threats to the continued safe operation of aircraft. As a result, the U.S. Air Force, the U.S. Navy, the Federal Aviation Administration (FAA), and the European Joint Aviation Authorities (JAA) have guidelines on how aircraft should be designed and maintained to minimize the risk of failure from fatigue damage [1–5]. Although corrosion has a deleterious impact on structural integrity, the airworthiness regulations and requirements have limited instructions regarding corrosion, noting that each part of the aircraft has to be “suitably protected against deterioration or loss of strength in service due to any cause, including weathering, corrosion and abrasion” [6, 7]. The ability to assess the impact of future corrosion on structural integrity, alone or acting in concert with fatigue, is difficult. A framework to assess the effects of corrosion in combination with fatigue on structural integrity has been under development [8].

The parameters of primary interest to aircraft fleet managers are:

- Risk of failure for a single component on a single aircraft
- Failure risk of an individual aircraft (the sum of risks for all components)
- Hazard failure rates for individual aircraft and the aircraft fleet
- Cost-effectiveness of maintenance actions in reducing failure risk for individual aircraft and the fleet

The purpose of this chapter is to review key aspects of assessing the quantitative risk to airframe structures from concurrent corrosion and fatigue damage. Both the current engineering practice and new research developments are reviewed. The physics-based stochastic damage models necessary to make this risk assessment as well as the statistical data needed to construct these models are discussed. The emphasis is on physics-based stochastic modeling of corrosion-fatigue damage. Lack of data and engineering understanding of the physics of a damage process are highlighted. At the end of the chapter, various probabilistic results computed for different physics-based stochastic damage models and different corrosion severity conditions are illustrated for a typical aircraft lap joint.

28.2 Current Engineering Philosophy

Aircraft-structure joints are the most fatigue- and corrosion-susceptible areas on an aircraft. Loads are transferred from one structural detail to another through fasteners, with the attendant stress-concentrating holes making this a prime location for fatigue cracks to form. The tight fit of details and fasteners can trap moisture in the joint. Relative movement between the structural details and the fasteners, as well as the stress concentrations, can cause corrosion protection systems (anodize, primer, and topcoat) to crack and wear, allowing moisture to reach the aluminum parts and start the corrosion process. A typical example structure is a longitudinal skin joint on the pressurized fuselage of a transport aircraft (Figure 28.1). The loading of longitudinal skin joints, particularly those on or near the horizontal neutral axis of the fuselage, is simply the pressurization of the fuselage, which is approximately constant amplitude with a stress ratio (ratio between minimum over maximum stress) of zero. For illustration purposes, we assume that there is only a single pressurization stress cycle per flight.

28.2.1 Deterministic Approach

In the current USAF practice, when the aircraft is designed, a crack-growth analysis is performed for each critical location assuming a discrete 1.27-mm (0.05 in.) flaw or crack (Figure 28.2). This conservative assumption protects against the possibility of a rogue flaw at any one of the critical locations resulting in the loss of an aircraft or its crew. Different assumptions are allowed if the critical location is a cold-worked hole or interference-fit fastener. But for illustration, we will work with the 1.27-mm crack. The existence of a 1.27-mm (0.05 in.) flaw is a rare event that happens less than one in a million based upon back calculations from full-scale fatigue-test crack data [9].

Each critical location is to be inspected at half the component life, determined by the crack-growth analysis, after approximately 11,000 pressurization cycles for the example in Figure 28.2. In principle, half the life was chosen in order to cover scatter from the “mean” life given by the analysis. The condition of the structure in terms of amounts and severities of cracking, corrosion, fretting, etc., is determined with nondestructive inspections (NDI). The inspection should be accomplished with an NDI method capable of finding a crack less than or equal to the analytical crack length at half the component life from a 1.27-mm flaw.

The capability of NDI to find cracks, or other types of damage, is expressed in terms of the probability of detection (POD) curve. POD curves for fatigue cracks in standard geometries have been developed and compiled in handbooks [10–12] for a variety of NDI methods. An example of a POD curve for eddy-current inspection of a Boeing 737 lap joint is shown in Figure 28.3. Note that 1.27-mm fatigue cracks in the joint were found only about 5% of the time with this particular NDI setup. The USAF philosophy is to assume

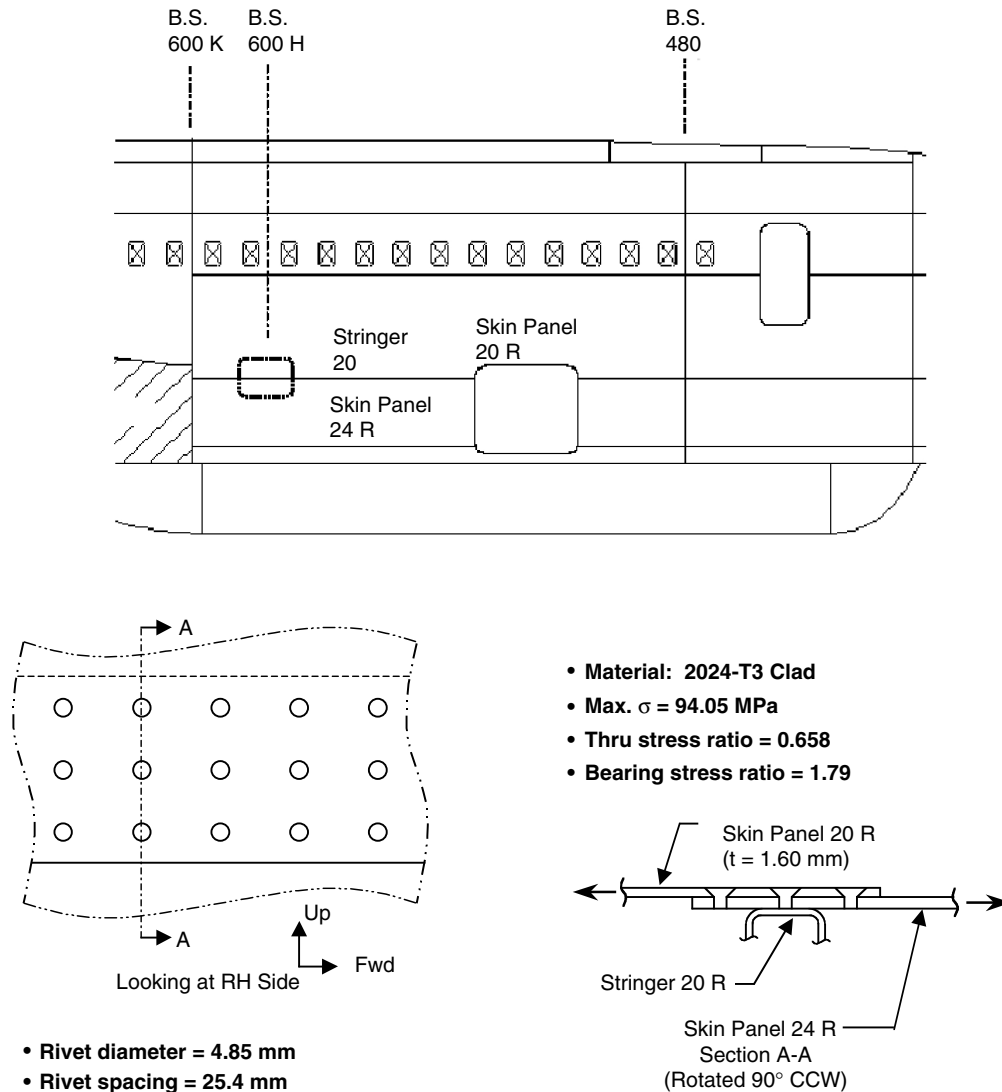


FIGURE 28.1 Details of joint selected as example.

after an inspection that there is a crack at the location just below the 90% detection with 95% confidence limit, denoted 90/95 value. For the aircraft splice joint in Figure 28.1, the 90/95 value of crack size is 2.39 mm, which would be adequate to find the almost 4-mm crack predicted for 1.27-mm starting crack at 11,000 hours (Figure 28.2). From the crack-growth analysis in Figure 28.2, it would take approximately 16,000 pressurization cycles for a 2.93-mm crack to grow to failure. Thus, if no cracks were found in the lap joint during the first inspection using the above eddy-current technique, the second inspection would need to be 8,000 cycles later, or after approximately 19,000 pressurization cycles. The times for subsequent inspections at this location are determined using this same procedure until a crack is found and repaired, or the aircraft is retired. After a repair, inspection intervals will be determined by the characteristics of the repair and its ability to prevent further damage and degradation to the structure. As an aircraft fleet becomes older, inspections can be required more frequently. These inspections can be a real burden to the maintainers and to the operators.

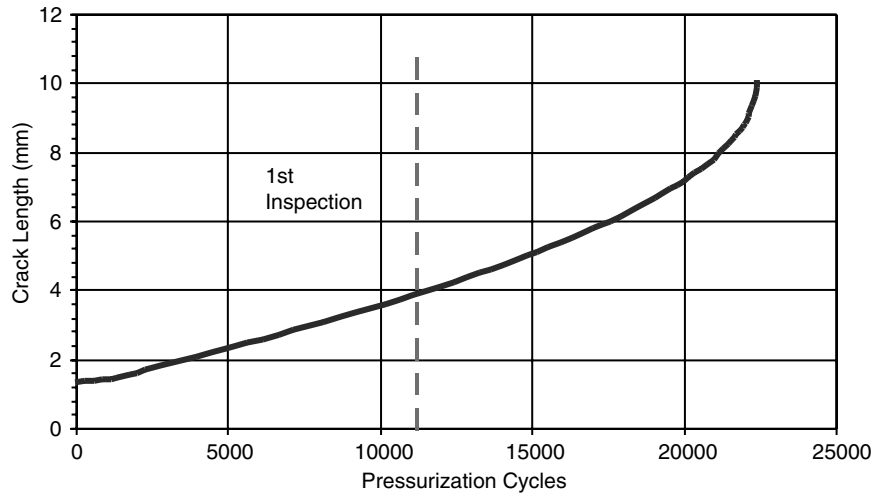


FIGURE 28.2 Example of crack-growth analysis and time to the first inspection.

Recent work has sought to quantify the capabilities of several NDI methods to find corrosion [13]. The major concern with NDI for corrosion is detecting corrosion that is buried between layers of built-up structure. Corrosion on a visible surface is best found visually in adequate lighting; however, this method does not reveal how deeply the corrosion penetrates. When looking for corrosion, the measured quantity is part thickness that is converted to thickness loss from the design specification. In general, eddy current and ultrasound are capable of determining the thickness of a part with reasonable accuracy when the accessible surface is uncorroded. A roughened surface due to corrosion creates difficulties for surface-contacting probes or probes that need an accurate standoff from the surface. X-rays can be used to measure part thickness with corrosion on either surface, provided that there is access to both sides of the part. The ability of any method to detect corrosion depends upon the size of the corroded area vs. the size of the area over which the NDI signal is averaged.

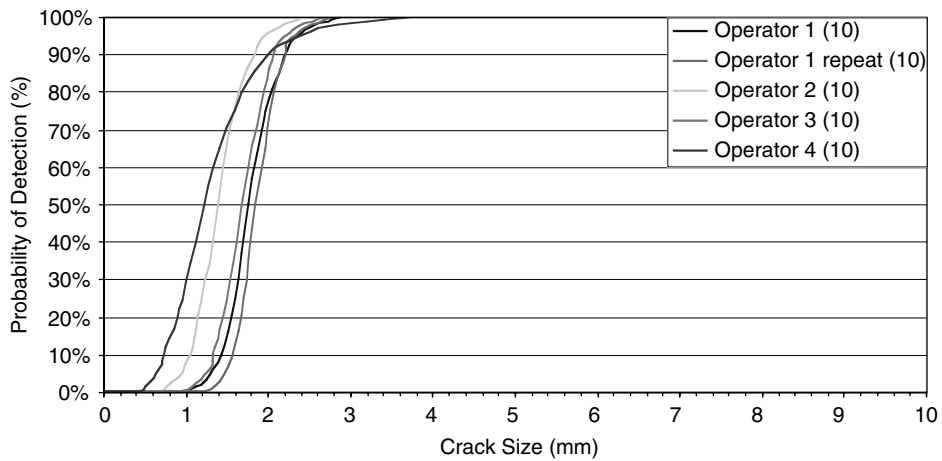


FIGURE 28.3 Results of probability-of-detection study for eddy-current inspection with 200-kHz probe of the fasteners in an unpainted 737 aluminum aircraft splice joint.

Multiple site damage (MSD) or widespread fatigue damage (WFD) should also be considered when evaluating failure risks of structural components. The above approach to aircraft maintenance was developed for discrete source damage, before the risks posed by MSD were fully recognized. The MSD scenario typically assumed when considering damage tolerance is a long, detectable crack emanating from a critical location with small, undetectable cracks at many of the adjacent fastener holes. These small cracks provide a low-energy path for the long crack to follow during fast fracture, much like perforations in paper make it easier to tear a sheet in a specific spot. This scenario cannot be identified with NDI. And the likelihood of MSD existing cannot be reliably estimated analytically because good models for estimating the distribution of small cracks in a structure do not exist. The issue of MSD will be left for another time, when it can be dealt with more thoroughly.

28.2.2 Risk-Based Approach

Typically, in order to determine the failure risk of an aircraft component, three pieces of information are needed:

1. The current “damage” condition of the component
2. The material capacity associated with the progressive “damage” mechanism, i.e., residual strength, or critical crack size, or fracture toughness
3. A predictive model of how the current “damage” condition will develop with continued usage

The maximum frequency of a structural failure leading to the loss of the aircraft acceptable to USAF is 10^{-7} event occurrences per flight [14, 15].

28.2.2.1 Risk-Based Condition Assessment

In a risk-based or risk-quantified approach to aircraft management, a distribution of crack sizes would be estimated, either analytically or based upon previous inspection experience, for a structure prior to an inspection. The crack size distribution would be modified after the inspection based upon the POD for the NDI method and the subsequent maintenance actions performed on the detected cracks.

Lincoln [15] discussed the utility of probabilistic approaches for assessing aircraft safety and for solving key reliability problems faced in practice, such as:

1. Potential-cracking problems are revealed, and the aircraft is beyond its deterministic damage-tolerance limits.
2. Aircraft cracking has occurred to the extent that the deterministic-damage-tolerance derived inspection intervals need to be shortened in order to preserve safety.
3. Aircraft have been designed to be fail safe, but (widespread) fatigue damage has degraded the aircraft structure such that the fail safety of the structure has been compromised.

One of the difficulties in managing aircraft fleets is tracking data from past aircraft inspections to refine the assessment of the current condition of each aircraft or the entire fleet. A good knowledge of the current state of a component or aircraft is important for accurately determining the risk of failure. Electronic databases make storing the data easier. The challenge is getting the data into the database.

Over the last decade, the USAF has developed the probability of fracture (PROF) software to compute the probability of a component fracturing during a single flight [16, 17]. Inputs to the program are based upon data that is readily available as a result of the USAF aircraft structural integrity program (ASIP). These inputs include: material fracture toughness, predicted crack size vs. flight hours for the usage spectrum, normalized stress intensity vs. crack length for the location of interest, distribution of crack sizes at that location throughout the fleet at some previous time, and the distribution of extreme loads the aircraft will experience.

PROF computes the single-flight probability of failure P_f by incorporating two independent failure events: (1) failure occurs when the effective crack size is larger than a prescribed maximum crack size (the residual strength of the component becomes unacceptably low), or (2) failure occurs when the

effective crack size is smaller than critical size, a_c , but the maximum stress intensity factor is larger than material fracture toughness, K_c :

$$P_f = \int_0^{a_c} f(a)[1 - \text{Prob}(K(a) \leq K_c)] da + [1 - \text{Prob}(a \leq a_c)] \quad (28.1)$$

where $f(a)$ is the crack-size distribution function and a_c is the critical crack size.

USAF is continuing to improve the methods used to determine the probability of fracture and risks associated with operational aircraft fleets.

28.2.2.2 Local Failure Criteria

The effect of selecting different local failure criteria on the stress–strain curve is shown in Figure 28.4. Since the material toughness can be related to a critical crack size at failure for a given stress, the two failure criteria in PROF can be plotted together on the crack size–stress plane as in Figure 28.5. The residual strength of the component defines the limit of a component's ability to carry load [18] and can be simplistically thought of as a limit surface in the stress vs. crack size plane described by the minimum of the yield and fracture curves in Figure 28.5. When the structure is new and the sizes of any cracks are small, the net section stress must be less than the yield strength of the material. For a longitudinal lap splice subjected to only pressurization loading (Figure 28.1), the maximum net section stress is $\sigma/(1 - nd/W)$, where W is the width of the panel, d is the diameter of the fastener holes, and n is the number of fasteners in a row. As the component is fatigued, cracks form and grow. The residual strength of the component is the stress required to cause fracture. For a single crack, based on linear elastic fracture mechanics (LEFM), the local stress at the crack tip that defines the residual stress can be simply computed by the relationship

$$\sigma_c = \frac{K_c}{\beta\sqrt{\pi a}} \quad (28.2)$$

where K_c is the critical stress intensity factor or fracture toughness that causes material to fracture, β is the stress intensity geometry factor for the given crack, and a is the crack size.

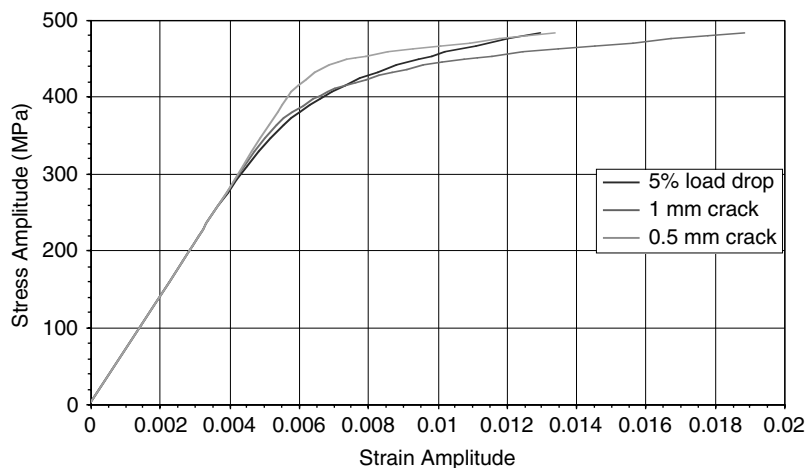


FIGURE 28.4 Cyclic stress–strain curve for 2024-T3 sheet.

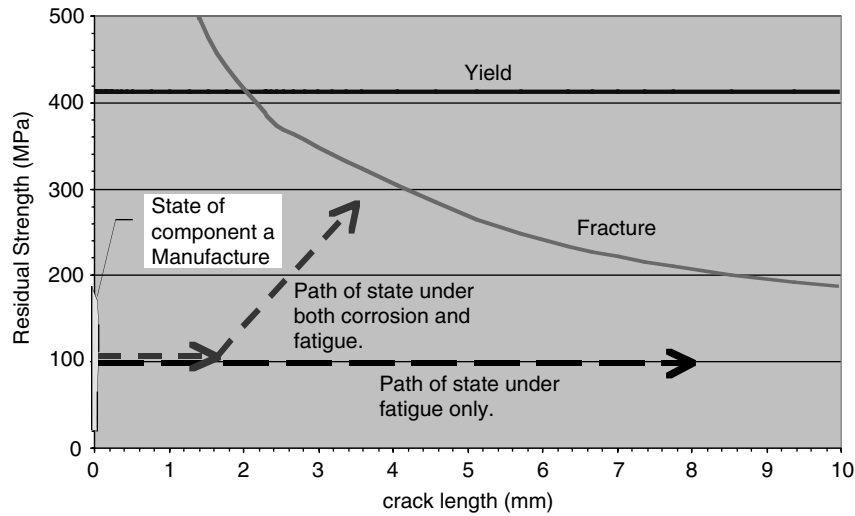


FIGURE 28.5 Pictorial description of residual strength space.

If the structure is designed such that load can be redistributed from the cracked component, or area of the component, to other components or areas, the determination of the critical stress for failure of the component is harder. As the component cracks, it becomes more compliant. Load redistributes to stiffer intact structure nearby, reducing the stress intensity at the crack and the likelihood that fast fracture will occur. Such structure is said to be fail safe.

Yield strength and K_{Ic} are variable from lot to lot and even locally within a given component; the limits in Figure 28.5 become zones of constant-probability contours. The values for yield strength used in aircraft design are based upon the A- or B-basis allowable in Mil-Hdbk-5 [19]. An A-basis allowable is the lower value of either a statistically calculated number or the specification minimum. The statistically calculated number indicates that at least 99% of the population is expected to equal or exceed the statistically calculated mechanical property value, with a confidence of 95%. A B-basis allowable indicates that at least 90% of the population of values is expected to equal or exceed the statistically calculated mechanical property value, with a confidence of 95%.

Plane-strain fracture toughness, K_{Ic} , is treated as being normally distributed, with mean values and standard deviations calculated on a rather small data set. However, the critical fracture toughness for a part, K_{Ic} , is dependent upon the thickness of the material. A number of K_{Ic} values are compiled by Skinn et al. [20] for 2024-T3 aluminum sheet. However, of over 140 tests reported, there were only 3 where the net section stress in the specimen did not exceed 80% of the yield strength and could be considered to have met the requirements of linear elastic fracture mechanics. The average of those three tests on 1.5-mm-thick sheets was $119.6 \text{ MPa}\sqrt{\text{m}}$, with a standard deviation of $9 \text{ MPa}\sqrt{\text{m}}$.

28.2.2.3 Uncertainty in Failure Criteria

In the above discussion of residual strength, failure is considered as a stepwise change of system state—from having structural integrity to having no structural integrity. In reality, the transition from a sound state to a “failed state” is smooth; the changes in system integrity occur gradually with small changes in time. It is difficult to define a distinct instant when “failure” occurred. Thus there is a lack of distinctness, or uncertainty, to the failure criteria. Several researchers have proposed using nondeterministic approaches, using either probabilistic or fuzzy approximation, to describe fatigue damage and subsequent failure [21, 22]. This approach has a certain appeal to it, but it still requires more development before being applied to practical situations.

28.3 Corrosion-Fatigue-Damage Modeling

At low homologous temperatures, fatigue damage accumulates with applied load cycles, regardless of how fast or slowly the cycles are applied. On the other hand, corrosion develops as a function of time, regardless of whether the structure is loaded or not. Putting these two mechanisms into the same model is challenging because of the different “time” scales at which “damage” develops.

28.3.1 Fatigue Damage

Fatigue changes crack size distribution as a result of applied loading only. A new structure starts out with few, if any, cracks. New cracks form at stress concentrations with applied loading as a result of local plasticity and microplasticity. Many microscopic cracks may form, but only a few become visible, macroscopic cracks. The portion of the fatigue life until the formation of a detectable crack, which is considered here to be about 2 mm, is denoted as crack nucleation. The portion of the fatigue life after a detectable crack is formed until the component fails is denoted as crack propagation or growth. Different mathematical models are used to analyze these two phases of the fatigue life, though it is likely that a single physical mechanism operates throughout the entire fatigue life [23].

28.3.1.1 Crack Initiation

A common model for estimating the load cycles until the development of a detectable crack is currently the semiempirical local strain-life approach [24–26]. The local strain-life method models the stress–strain history at the “root” of a stress concentration, or notch, from the cyclic stress–strain curve of the material and the notch (local plasticity) analysis. The number of constant-amplitude stress–strain (closed) cycles that is accumulated until the detectable crack size is reached is determined based on the strain-life curve of the material adjusted for the nonzero mean stress effects. For variable-amplitude cycle loading, the cumulative damage defined by crack size is then computed using the kinetic damage equation. To count stress–strain cycles, rainflow counting or other methods can be used. The growth and linkup of small cracks is included in crack initiation when the models are calibrated to the detection of a suitably long crack, so models for small crack growth are not needed.

The material for the aircraft structural joint shown in Figure 28.1 is 2024-T3 aluminum sheet. Examples of cyclic stress–strain curves for this material, found by putting a curve through tips of the stable hysteresis loops obtained during strain-controlled fatigue tests of smooth specimens, are shown in Figure 28.4. The differences between the curves are partially the result of using different failure criteria for the fatigue tests, which results in the hysteresis loops being defined as stable at different times [27]. Hysteresis loops are considered stable at half the cycles to failure. However, an alloy like 2024-T3, which is cold-worked prior to aging, can cyclically soften, i.e., the extreme stresses experienced at the extreme strain points decrease with increasing number of load cycles throughout the entire test, making the determination of the stable hysteresis loop somewhat imprecise.

The curve can be modeled using the Ramberg-Osgood equation

$$\frac{\Delta\epsilon}{2} = \frac{\Delta\sigma}{2E} + \left(\frac{\Delta\sigma}{2K'} \right)^{\frac{1}{n'}} \quad (28.3)$$

where $\Delta\epsilon/2$ is the strain amplitude, $\Delta\sigma/2$ is the stress amplitude, E is the elastic modulus, K' is the cyclic strain hardening coefficient, and n' is the cyclic strain hardening exponent. The values of K' and n' for the different curves are provided in Table 28.1 [27].

For the aircraft lap joint shown in Figure 28.1, a detailed analysis of the load transfer indicates that the most critical location is the first row of fasteners in the outer skin. It has the largest bypass, or through, stress, 61.9 MPa, and the largest bearing stress, 168.3 MPa. Applying the respective stress concentration factors for a hole in a plate [28] and adding the components together gives the maximum $K_t\sigma = 417.4$ MPa. The local stress–strain history can be determined by a finite-element analysis, which can be very time

TABLE 28.1 Cyclic Strain Hardening Coefficients and Exponents for Curves in Figure 28.4

Curve (Failure Criterion)	K' (MPa)	n'
5% load drop	843	0.109
1-mm crack	669	0.074
0.5-mm crack	590.6	0.040

consuming if the load history has a large number of load levels in it, or by using Neuber's equation, $K_t^2 = K_\sigma K_\epsilon$, where K_σ is the stress concentration factor, $\sigma_{\text{notch}}/\sigma_{\text{global}}$, and K_ϵ is the strain concentration factor at the hole, $\epsilon_{\text{notch}}/\epsilon_{\text{global}}$. Solving for the maximum notch stress and strain yields the results in Table 28.2 for each of the cyclic stress-strain curves.

The strain amplitude and mean stress (or the maximum stress) are used to estimate the time to a detectable crack. First, the strain-life curve, determined with data from $R = -1$ (completely reversed) strain-control testing, is needed. The standard strain-life curve expresses alternating strain as a function of cycle life:

$$\epsilon_a = \frac{\Delta\epsilon}{2} = \frac{\sigma'_f}{E}(2N_f)^b + \epsilon'_f(2N_f)^c \quad (28.4)$$

Values of the coefficients and exponents for 2024-T3 using the three failure criteria above are listed in Table 28.3 [27]. The first term in Equation 28.4 characterizes high-cycle fatigue when macroscopic plastic deformation is not evident, while the second term characterizes low-cycle fatigue associated with macroscopic plastic deformation. The resulting strain-life curves are compared in Figure 28.6. The abscissa of the strain-life curves represent the number of applied load cycles at which 50% of the specimens tested at that strain amplitude would have failed.

The strain-life curves are for completely reversed loading with a zero mean stress. The loading for the fuselage lap joint has a stress ratio of zero, i.e., a mean stress of $\Delta\sigma/2$. So the strain-life curves need to be adjusted for a nonzero mean stress.

For evaluating the probabilistic crack initiation life, a local strain-life approach with randomized strain-life curve parameters can be used. Thus, the four parameters, σ'_f , b , ϵ'_f , and c , are random material parameters. It is expected that the first pair of parameters that influences the short lives is statistically independent with respect to the second pair of parameters that influences the long lives. Within each of the two pairs of parameters, there is expected to be a certain level of statistical dependence.

The most popular numerical procedures used to correct the strain-life curve for the nonzero mean stress effects are [29]:

1. Morrow correction (MC): mean-stress effect in the elastic term

$$\epsilon_a = \frac{\sigma'_f}{E} \left(1 - \frac{\sigma_m}{\sigma'_f} \right) (2N_f)^b + \epsilon'_f (2N_f)^c \quad (28.5)$$

TABLE 28.2 Notch Stress and Strain History for the First Row of Fasteners in the Joint of Figure 28.1

Curve (Failure Criterion)	σ_{max} (MPa)	$\Delta\epsilon/2$	σ_{mean} (MPa)
5% load drop	388.7	0.00276	194.4
1-mm crack	392.3	0.00279	196.2
0.5-mm crack	412.8	0.00294	206.4

TABLE 28.3 Strain-Life Equation Coefficients and Exponents for 2024-T3 Sheet

Strain-Life Curve (Failure Criterion)	σ'_f (MPa)	B	ϵ'_f	c
5% load drop	835	-0.096	0.174	-0.644
1-mm crack	891	-0.103	4.206	-1.056
0.5-mm crack	1044	-0.114	1.765	-0.927

2. Modified Morrow correction (MMC): the mean-stress effect in the elastic and plastic strain terms

$$\epsilon_a = \frac{\sigma'_f}{E} \left(1 - \frac{\sigma_m}{\sigma'_f} \right) (2N_f)^b + \epsilon'_f \left(1 - \frac{\sigma_m}{\sigma'_f} \right)^{\frac{c}{b}} (2N_f) \quad (28.6)$$

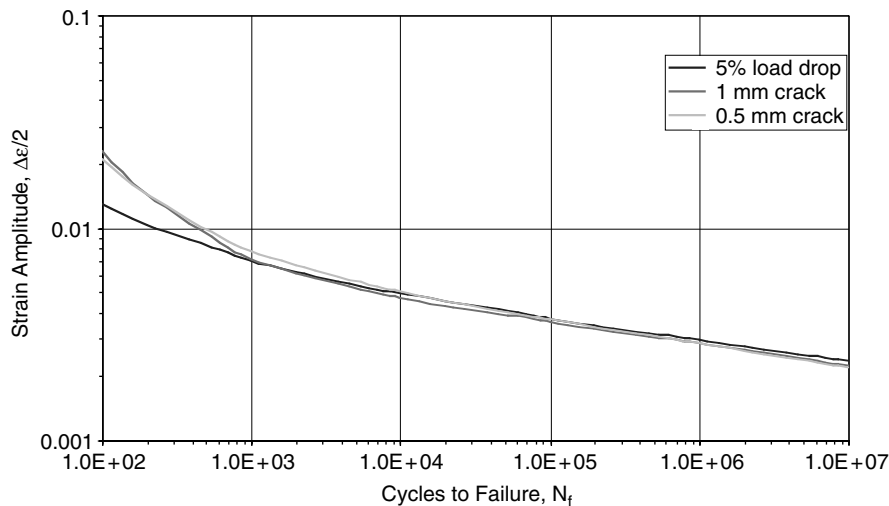
3. Smiths-Watson-Topper (SWT) approach changes the strain-life curve expression by

$$\sigma_{\max} \epsilon_a = \frac{(\sigma'_f)^2}{E} (2N_f)^{2b} + \sigma'_f \epsilon'_f (2N_f)^{b+c} \quad (28.7)$$

The mean and maximum stresses are denoted by σ_m and σ_{\max} in the above equations. It should be noted that the selection of the mean-stress correction procedure has a large impact on the computed component lives.

For the 2024-T3 sheet material, the adjusted strain-life curves using MC procedure are compared in Figure 28.7. The range of strain amplitudes in Table 28.2 produces estimates of the time to 50% of the fastener holes in the first row having a detectable crack as 100,000 to 150,000 pressurization cycles.

If the loading stress history is variable amplitude instead of constant amplitude, then rainflow, range pair, or other cycle-counting procedures can be used to break the local stress-strain history into applied closed stress-strain cycles of different strain amplitudes, $\Delta\epsilon/2$, and mean stresses, σ_m .

**FIGURE 28.6** Strain-life curves for 2024-T3 sheet.

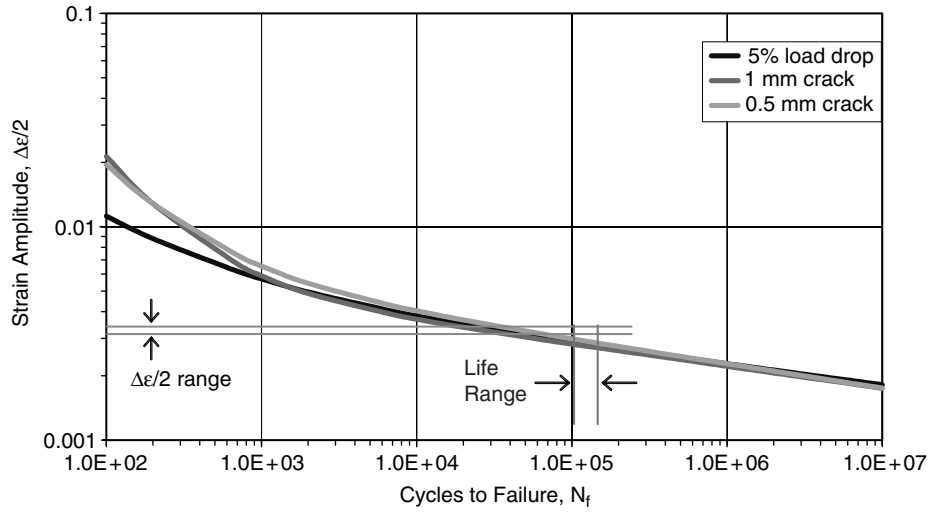


FIGURE 28.7 2024-T3 sheet strain-life curves adjusted for $R = 0$ loading with Morrow's equation.

For every cycle in the history, the number of cycles to failure of a smooth specimen under constant-amplitude loading is determined by solving Morrow's equation for N_f . Then, the cumulative damage is computed by solving the first-order differential kinetic damage equation of the form:

$$\frac{dD}{dN} = f(D, N, N_f(\epsilon_a, \sigma_m), p) \quad (28.8)$$

where the letter p denotes the physical parameters of the cumulative damage model.

The total accumulated damage, D_T , due to cyclic loading can be directly computed by the convolution of the damage function, $D(X_{\min}, X_{\max})$, with cycle counting distribution $N_T(X_{\min}, X_{\max})$:

$$D_T = \int_T d(t) dt = \sum_{i \text{ for } v \leq u} D(v, u) = - \iint_{v \leq u} N_T(v, u) \frac{\partial^2 D(v, u)}{\partial v \partial u} dv du \quad (28.9)$$

The integral value is the summation of all elementary damages produced by the sequence of closed stress-strain hysteresis loops.

It was proven experimentally by Halford [30] that for a sequence of cycles with constant alternating stress and mean stress, the cumulative damage curve, the crack initiation life, $N_f(\epsilon_m, \sigma_m)$, can be accurately constructed based only on two experiments for the extreme amplitude levels, i.e., maximum and minimum life levels. The greater the ratio between the (two) extreme life levels, the more severe damage interaction there is and the greater deviation from the linear-damage rule.

28.3.1.1.1 Linear-Damage Rule

The popular linear-damage rule (LDR) has the mathematical form:

$$D = \sum \frac{n_i}{N_i} = \sum r_i \quad (28.10)$$

where D is the damage, n_i is the number of cycles of i th load level, N_i is the fatigue life according the i th load level, and r_i is the cycle ratio of i th load level. In the linear-damage rule, the damage is measured by the cycle ratio. Failure occurs when the damage reaches unity.

The shortcoming of the popular linear-damage rule (LDR) or Miner's rule is its stress independence or load-sequence independence; it is incapable of taking into account the interaction of different load levels. There is substantial experimental evidence that shows that LDR is conservative under completely reversed loading condition for low-to-high loading sequences, $\sum r_i > 1.0$, and severely under conservative for high-to-low loading sequence, $\sum r_i < 1.0$. It should be noted that for intermittent low-high-low-high- ... -low-high cyclic loading, the LDR severely underestimated the predicted life, as indicated by Halford [30].

28.3.1.1.2 Damage Curve Approach

The damage curve approach (DCA) was developed by Manson and Halford [30]. The damage curve is expressed in the following form:

$$D = \left(\frac{n}{N}\right)^q = \left(\frac{n}{N}\right)^{\left(\frac{N}{N_{\text{ref}}}\right)^\beta} \quad (28.11)$$

where D is the accumulated damage, n is the number of cycles, and N is the fatigue life for the corresponding strain amplitude and mean stress. N_{ref} is the *reference* fatigue life. Parameter β is set equal to 0.40 for many alloys.

28.3.1.1.3 Double Damage Curve Approach

The double damage curve approach (DDCA) was developed by Manson and Halford by adding a linear term to the DCA equation [30]. The DDCA is defined by the relationship:

$$D = \left(\frac{n}{N}\right) \left[q_1^\gamma + (1 - q_1^\gamma) \left(\frac{n}{N}\right)^{\gamma(q_2 - 1)} \right]^{1/\gamma} \quad (28.12)$$

where

$$q_1 = \frac{0.35 \left(\frac{N_{\text{ref}}}{N}\right)^\alpha}{1 - 0.65 \left(\frac{N_{\text{ref}}}{N}\right)^\alpha}, \quad q_2 = \left(\frac{N}{N_{\text{ref}}}\right)^\beta$$

The parameters α and β are set to equal 0.25 and 0.40, respectively, for many alloys. Parameter study shows that the value of γ can be set at 5.00, which makes DCA a sufficiently close fit to DDCA. From the equations of DCA and DDCA, it can be seen that the exponent q in DCA and the parameters q_1 and q_2 are all stress-level dependent, and the interaction between different stress-levels can be adequately considered.

28.3.1.1.4 Stochastic Variability in Crack Initiation

Cracks nucleate in aluminum alloys at coarse slip bands inside large grains, with primary crystallographic slip planes oriented favorably to the applied loading so that there is microplastic deformation around large, hard constituent particles (or other phases), or at grain boundaries [31–38]. Variability in grain orientations and sizes and in particle sizes leads to variability in the time to nucleate a crack.

One source of data for crack nucleation in 2042-T3 is the results of the AGARD round cooperative test program for short-crack growth-rate data [32]. The number of cycles until a through crack developed was reported for many of the specimens. The specimens were 2.3 mm thick. The size is consistent with the definition of crack initiation stated earlier, so these data can provide an estimate of the scatter in the time to form a 2-mm crack. Single-edge notched tension (SENT) specimens shown in Figure 28.8 were used.

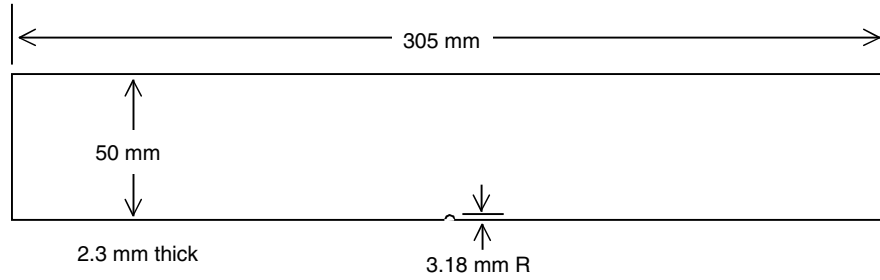


FIGURE 28.8 Single-edge notched tension specimen used in AGARD short-crack cooperative test program. (From Newman, J.C., Jr. and Edwards, P.R., Short-Crack Growth Behaviour in an Aluminum Alloy: an AGARD Cooperative Test Programme, AGARD R-732, 1988. With permission.)

Tests were conducted with constant-amplitude loading at three different maximum stress levels for each stress ratio, R , of -2 , -1 , 0 , and 0.5 . In addition, tests were carried out at three reference stress levels for two different load spectra: FALSTAFF (a standardized spectrum representative of the load-time history in the lower wing skin near the root of a fighter aircraft) and a Gaussian-type random load sequence. An example of the data along with cycles to initiation estimates using the three strain-life models is shown in Figure 28.9 for the constant-amplitude $R = 0$ tests.

Another useful data set for the variation in crack initiation time was done at Boeing in the 1970s [39]. The goal of the study was to develop sufficient fatigue data to identify the form of the life distributions, so that a probabilistic fatigue design method could be explored. Eight 2024-T3 panels, 914.4 mm wide by 3.18 mm thick, with 110 holes measuring 4.76 mm in diameter, were fatigue-tested under two different load spectra. The panels came from three different heats of material. A conductive-paint crack-detection circuit was used to detect cracks on the order of 0.5 mm from each hole. When a hole cracked, it was oversized to 9.53-mm diameter and cold-worked to inactivate that hole as a future crack site. Testing was continued until 10% to 20% of the holes had cracked, though in two instances testing continued until 50% of the holes cracked. The number of spectrum load points until crack detection during these tests is shown in Figure 28.10. The number for spectrum load points to cracking predicted with the

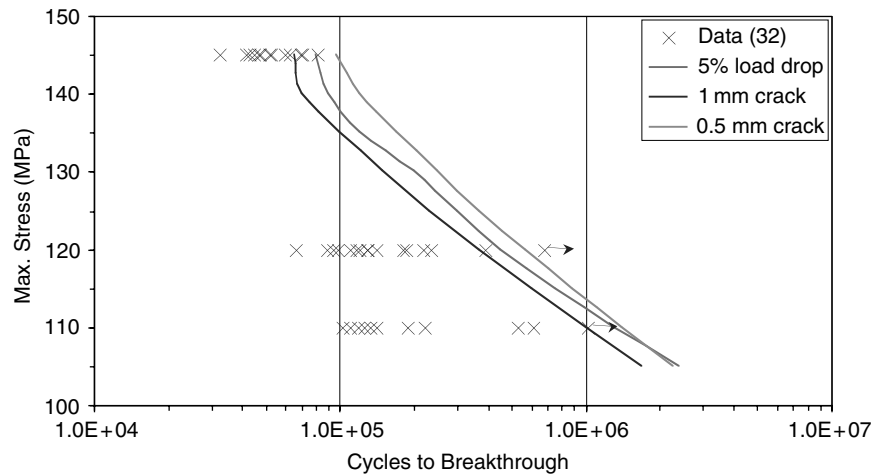


FIGURE 28.9 Cycles to development of a through-thickness crack in SENT specimens of 2024-T3.

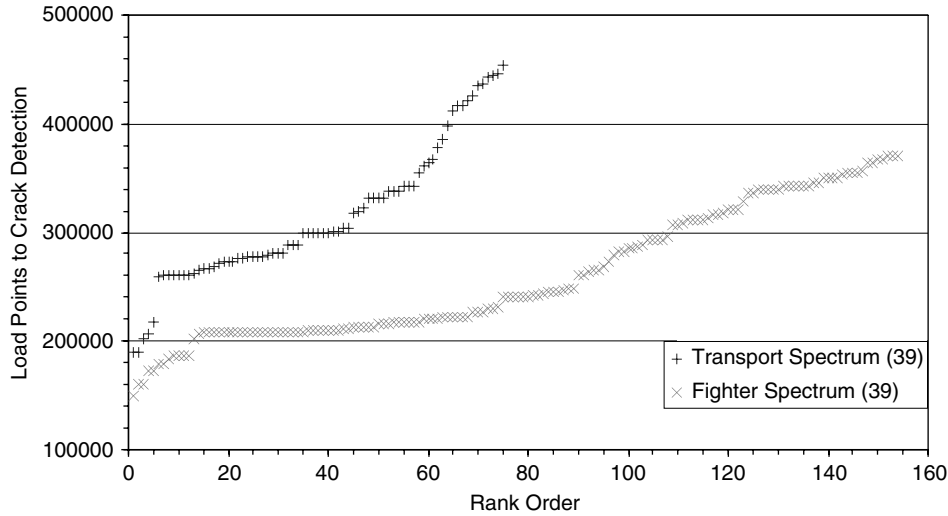


FIGURE 28.10 Cycles to detection of a crack at holes in 2024-T3 panels.

strain-life models presented earlier is approximately 1 million for the transport spectrum and about 440,000 for the fighter spectrum.

It should be noted that the most important source of uncertainty in probabilistic crack initiation life prediction comes from the strain-life curve uncertainty. The uncertainty in the shape of the damage curve model is of secondary significance in risk predictions.

28.3.1.2 Crack Propagation

Usually, in practice, the fatigue-crack-propagation models are based on linear elastic fracture mechanics (LEFM) theory. The limitation of the crack-propagation models based on LEFM theory is that they are applicable only to the propagation of long cracks. The small-crack growth below a given stress-intensity-range threshold is totally ignored. In fact, this is not true. Cracks nucleate at a microscale within the grains in plastic slip bands, and then, by accumulating strain energy, they penetrate the grain boundaries and start growing much faster. At each grain boundary there is potential for different crystallographic grain orientations in adjoining grains. If there is a significant difference in orientation, the small crack will stop until it can reform in the next grain. When many grains are penetrated and the crack is 1 to 2 mm, the crack becomes a long crack. Or in other words, a macrocrack was initiated. In the small-crack stage, the LEFM theory is not applicable, since the crack tip plastic zone occupies a large volume in comparison with the crack dimensions.

In this section, small-crack-growth modeling is covered by the cumulative damage models described earlier for crack initiation. No further discussion on the small-crack growth using micro- and meso-mechanics models is included here.

The rate of growth for long cracks, da/dN , is modeled as a function of the stress intensity range, ΔK , and some material behavior parameters. Crack size is denoted by its length, a , such that the current intensity of growth is uniquely defined by the increment per cycle or the crack growth rate, da/dN , expressed by a functional relationship of the form

$$da/dN = f(\Delta K, K_{\max}, K_c, \Delta K_{\text{th}}, E, \nu, \sigma_Y, \sigma_U, \epsilon_d, m) \quad (28.13)$$

where independent variables ΔK and K_{\max} define the stress intensity range and maximum stress intensity, respectively, and E (elastic modulus), ν (Poisson's ratio), σ_Y (yield strength), σ_u (ultimate

TABLE 28.4 Forman Equation Parameters for 2024-T3 Sheet

K_c (MPa√m)	C (mm/cycle)	m	n	p	Q
97.7	1.47×10^{-4}	0.39	1.66	0.93	0.54
R	0	0.5	0.7	-1	
ΔK_{th}	3.0	1.75	1.18	5.85	

strength), ϵ_d (ductility), m (hardening exponent), K_c (fracture toughness), and ΔK_{th} (threshold level) define the material properties. Several curve fits have been used to model empirical crack propagation.

28.3.1.2.1 Forman Model

One of the popular crack-propagation models is the generalized Forman fatigue-crack-growth model [40]:

$$\frac{da}{dN} = \frac{C(1 - R)^m (\Delta K - \Delta K_{th})^p (\Delta K)^n}{((1 - R)K_c - \Delta K)^q} \tag{28.14}$$

where R is the stress ratio, $\sigma_{min}/\sigma_{max}$; K_c is the critical stress intensity to cause fracture; ΔK_{th} is the threshold stress intensity as a function of the stress ratio; and C , m , n , p , and q are parameters used to fit the data. The values of the parameters for 2024-T3 sheet, based on data from 1.6- to 2.29-mm-thick sheet tested in lab air, dry air, or humid air, are given in Table 28.4, and the resulting crack growth-rate curves are shown in Figure 28.11.

The generalized Forman model describes the crack-growth behavior in all of the growth rate regimes. In the Region II, the above reduces to a linear equation in log-log space (Paris law).

The stochastic crack-growth model considers all the parameters as random quantities, but will include also two additional random factors for modeling uncertainties in the regions of low and high values of the rate da/dN in Regions I and III [40]:

$$\frac{da}{dN} = \frac{C(1 - R)^m \Delta K^n (\Delta K - \lambda_{K_{th}} \Delta K_{th})^p}{[(1 - R)\lambda_{K_c} K_c - \Delta K]^q} \tag{28.15}$$

The threshold random factor can be adjusted to simulate the uncertain small-crack growth.

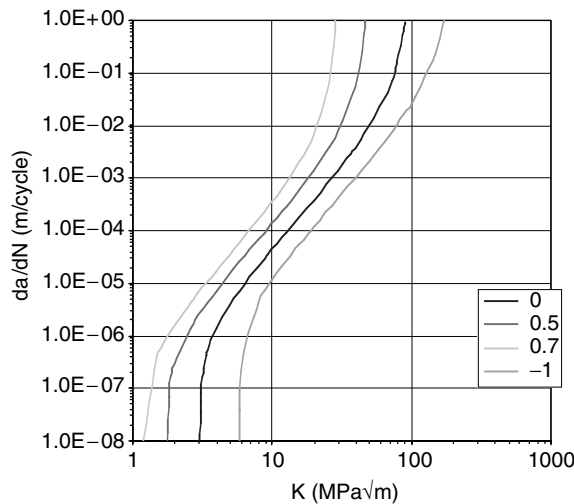


FIGURE 28.11 Corrosion rates for 2024-T3 sheet (1.63 mm thick) at four sites.

28.3.1.2.2 Hyperbolic Sine Model

The hyperbolic sine equation (SINH) model was developed by Pratt and Whitney Aircraft [41] to interpolate the crack-growth-rate data over a range of the four test variables T (temperature), R (stress ratio), F (frequency), and t_h (hold times). The SINH equation, which provides the basic sigmoidal shape and the constants to vary the shape of the curve and the inflection point, is given by the expression

$$\log(da/dN) = C_1 \sinh\{C_2[\log(\Delta K) + C_3]\} + C_4 \quad (28.16)$$

where da/dN is the crack growth rate per cycle, and ΔK is the stress-intensity-factor range. Parameters C_1 and C_2 are shape factors that “stretch” the curve vertically or horizontally, respectively, while C_3 and C_4 locate the inflection point horizontally and vertically, respectively. The slope of the curve at the inflection point is found to be $C_1 C_2$. The parameter C_1 is normally set to be 0.5 for many materials.

28.3.1.2.3 Modified Sigmoidal Model

The modified sigmoidal equation (MSE) model was developed by General Electric Company [41]. The basic MSE model is expressed as

$$\frac{da}{dN} = e^B \left(\frac{\Delta K}{\Delta K^*} \right)^P \left(\ln \left(\frac{\Delta K}{\Delta K^*} \right) \right)^Q \left(\ln \left(\frac{\Delta K_c}{\Delta K} \right) \right)^D \quad (28.17)$$

where da/dN is the crack growth rate per cycle, and ΔK is the stress intensity range. The equation has the general sigmoidal shape, with the lower asymptote ΔK^* representing the threshold value of ΔK . The equation involves six parameters, ΔK^* , ΔK_c , B , P , Q , and D . The parameter B controls the vertical motion of the entire curve. The parameter P provides the control of the slope at the inflection point of the sigmoidal curve. The vertical location of the inflection point is controlled by a combination of B , P , and ΔK^* .

28.3.1.2.4 Crack-Closure Model

A crack-propagation model based on crack-closure concepts was implemented in the FASTRAN code by Newman [42]. FASTRAN has been used to model small-crack propagation as well as long-crack propagation. However, the FASTRAN model does not capture the effects of material microstructure on small cracks, e.g., the grain boundary effects on small-crack growth rates and orientation at the tip. FASTRAN has, however, been successfully used by different researchers to assess the fatigue life of aircraft components, starting from the initial size of a constituent particle to the final fatigue failure [43, 44].

The analytical crack-closure model is used to calculate crack-opening stresses (S_0) as a function of crack-length and load history. Based on the value of the crack-opening stress, the effective stress-intensity-factor range is computed, and consequently the crack growth rates are determined. The crack-propagation equation in FASTRAN [44] is

$$\frac{dc}{dN} = C_1 \Delta K_{\text{eff}}^{C_2} \frac{1 - \left(\frac{\Delta K_0}{\Delta K_{\text{eff}}} \right)^2}{1 - \left(\frac{K_{\text{max}}}{C_5} \right)^2} \quad (28.18)$$

where

$$\Delta K_0 = C_3 \left(1 - C_4 \frac{S_0}{S_{\text{max}}} \right) \quad K_{\text{max}} = S_{\text{max}} \sqrt{\pi c} F \quad \text{and} \quad \Delta K_{\text{eff}} = (S_{\text{max}} - S_0) \sqrt{\pi c} F$$

The crack-opening stress, S_0 , is calculated from the analytical closure model. ΔK_{eff} is called effective stress intensity. ΔK_0 is the effective threshold stress-intensity-factor range. One of the advantages of using effective stress intensity is that the constants do not change at different stress ratios.

28.3.1.2.5 Stochastic Variability in Crack Propagation

The variability of fatigue-crack growth rate (FCGR) in aluminum alloys arises from changes in crystallographic texture along the crack path, the presence of microcracking at second-phase particles ahead of the crack, and the amount of transgranular vs. intergranular cracking. A significant data set for determining the variability in FCGR of 2024-T3 was produced by Virkler et al. [45]. Sixty-eight center-crack panels, 558.8 mm long by 152.4 mm wide, were cut from 2.54-mm-thick 2024-T3 sheet. Cracks were nucleated at a 2.54-mm-long electrodischarge-machined notch in the center of the panel and grown to 9.00 mm under controlled loading and environment. The number of cycles to reach specific crack lengths was then recorded for each panel under constant-amplitude ($R = 0.2$) loading with a maximum load of 23.4 kN at 20 Hz. Crack length vs. cycles data from a few select panels are presented in Figure 28.12 so that the individual curves can be identified more easily. The crack growth curves spread out as the cracks get longer, but they also cross each other in many places as a result of sudden increases and decreases in the growth rates. The corresponding FCGR data are plotted in Figure 28.13.

These data were generated at a single stress ratio; the scatter in crack growth rate data at other stress ratios may be different. In addition, the material was from a single lot. Lot-to-lot variations cannot be determined from these data. An estimate of the variation possible between different batches of materials can be made by comparing data collected from different test programs. Even then, the comparison is only over a limited range of stress intensities for a few stress ratios, and there are typically only a handful of specimens tested at each condition in any given program. An example of the data available from different test programs is compared with the curve given by the Forman equation in Figure 28.14 for $R = 0$ loading, which is of the most interest for the fuselage joint example.

It should be noted that, in Figure 28.12, the curves for crack length vs. load cycles have slightly different shapes, since the curves cross over. This indicates that an accurate probabilistic modeling would need to consider the random variation of the crack size evolution shapes. Typical stochastic crack-growth models [46]

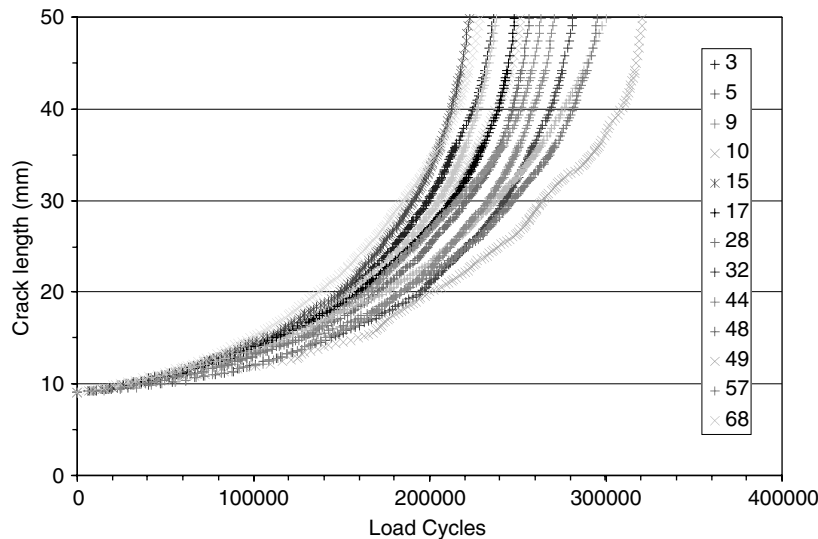


FIGURE 28.12 Crack length vs. load cycles for 2024-T3 sheet; $R = 0.2$, $P_{\text{max}} = 23.4$ kN. (Data from Virkler, D.A., Hillberry, B.M., and Goel, P.K., *The Statistical Nature of Fatigue Crack Propagation*, AFFDL-TR-78-43 [also DTIC ADA056912], 1978.)

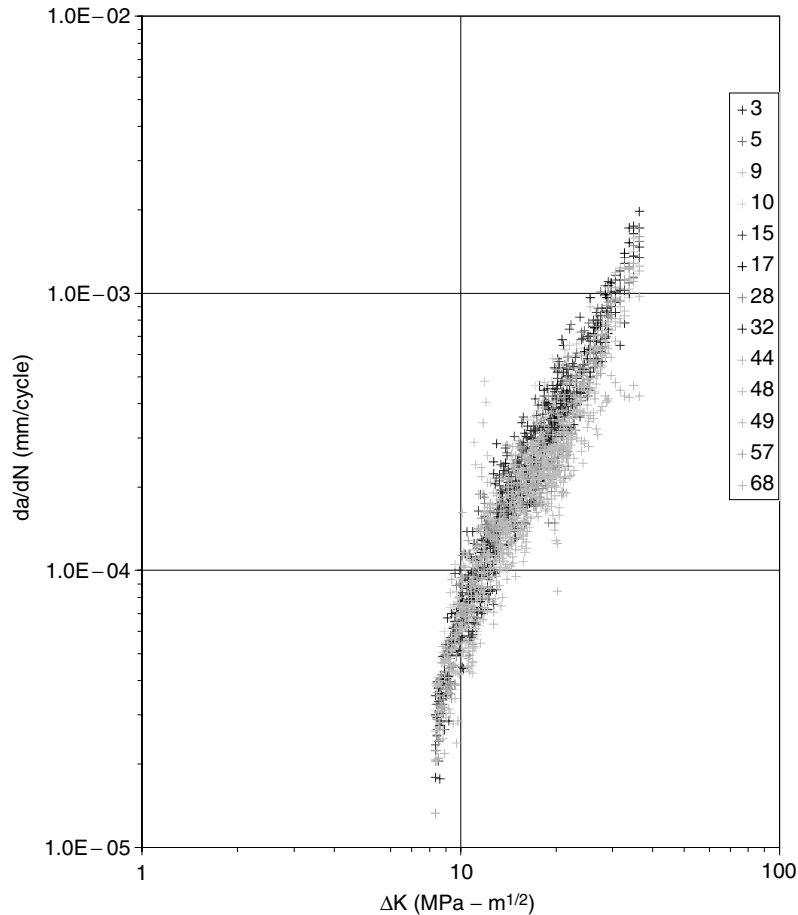


FIGURE 28.13 Fatigue-crack growth rate from curves in Figure 28.12.

assume that stochastic crack growth is composed of a median growth curve scaled by a positive random factor, neglecting the random fluctuating variations around the median shape. However, for a refined stochastic modeling, the crack growth process has to be idealized by a stochastic-process model rather than a random-variable model. The random shape variations indicate that the crack growth process has a finite correlation length. Correlation length is the distance for which the correlation between two points becomes lower than a threshold value. An infinite correlation length corresponds to a random-variable model.

Table 28.5 shows the statistics of number of cycles for four levels of crack sizes: 9.2 mm (close to initial flaw size of 9 mm), 14 mm, 29 mm, and 49.8 mm (considered critical crack size).

As shown in Table 28.5, between the random number of cycles measured for a 9.2-mm crack size and that measured for a 49.8-mm crack size, there is a correlation coefficient as low as 0.31. This indicates a relatively large departure from the usual perfect correlation or, equivalently, the infinite correlation length assumption.

Figure 28.15 shows the histograms from the Virkler data of the number of cycles at which the specified crack length was reached for two selected crack lengths. The numbers of cycles for two specimens are marked on the histogram plots with circles. It should be noted that the two specimens have crack evolutions that are quite different than other statistical crack evolutions. The position of the first specimen moves within the histogram of the crack population from a value in the far right tail at 9.2-mm crack size to a value close the mean at 49.8-mm crack size. The position of the second specimen moves from a value close to the mean at 9.2-mm crack size to a value in the far left tail at 49.8-mm crack size (it is

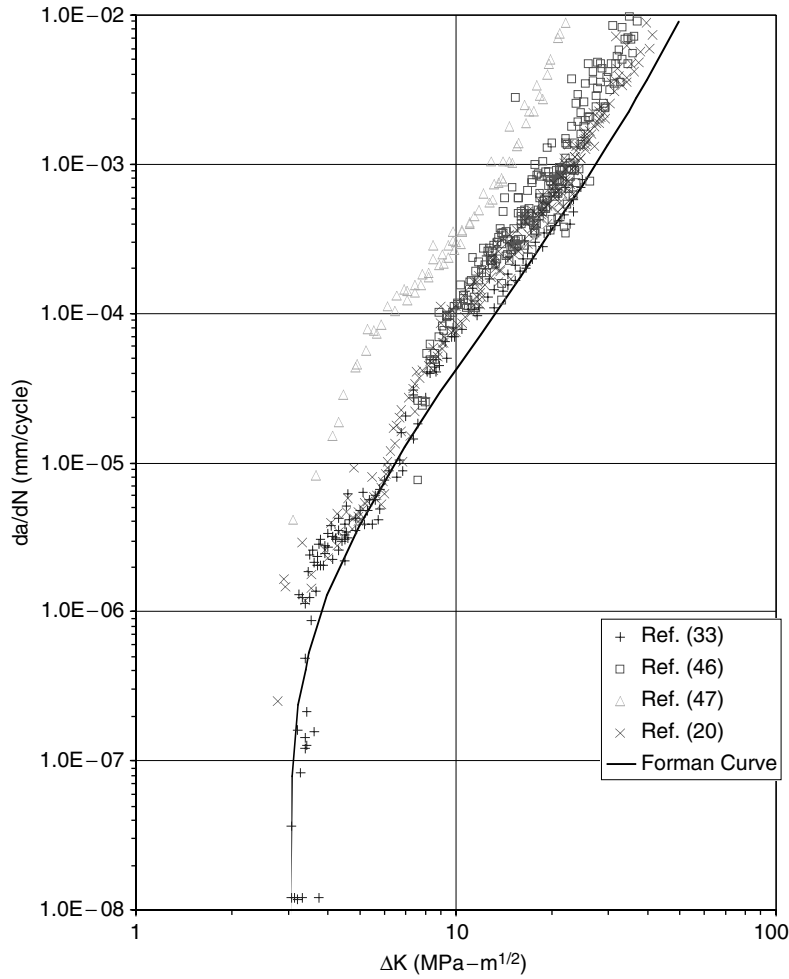


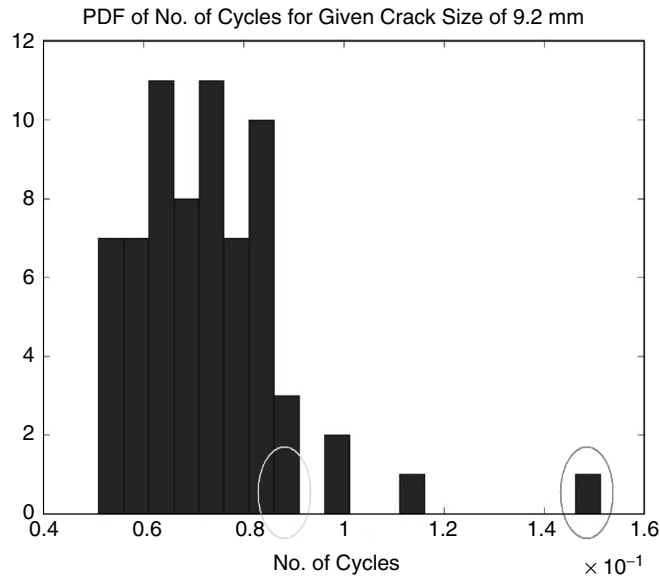
FIGURE 28.14 2024-T3 FCGR lot-to-lot variability, R = 0 loading.

the shortest-life crack path within the 68-specimen population). If there was a real perfect correlation between the random number of cycles measured at different crack lengths, then the two marked crack trajectories should maintain their position within the histogram of the crack population without migrating from one location to another.

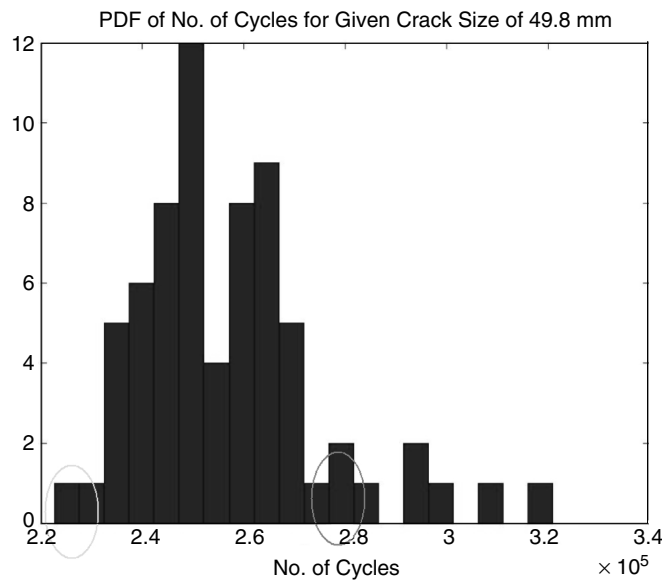
The fact that the correlation for length of the crack growth process is not infinite adds more complexity to stochastic modeling of crack-propagation physics. For a constant-amplitude stress-cycle loading, the changes in the shape of the crack growth curve are a consequence of the local nonhomogeneities in the

TABLE 28.5 Statistics for the Number of Cycles for a Given Crack Size

Crack Size	Mean	Standard Deviation	C.O.V.	Correlation w/9.2 mm	Correlation w/14.0 mm	Correlation w/29.0 mm	Correlation w/49.8 mm
9.2 mm	7,304	1,560	0.210	1.00	0.52	0.38	0.31
14 mm	105,976	9,863	0.093	0.52	1.00	0.87	0.78
29 mm	212,411	14,252	0.067	0.38	0.87	1.00	0.96
49.8 mm	257,698	18,850	0.073	0.31	0.78	0.96	1.00



(a) 9.2 mm



(a) 49.8 mm

FIGURE 28.15 Histograms of number of cycles for given crack length: (a) 9.2 mm; (b) 49.8 mm.

material properties and resistance against crack growth. For random-amplitude loading, the changes in the shape of the crack growth curve are larger, since they also include the effects of the random fluctuation of the stress amplitude. The random effects due to material nonhomogeneity and variation in loading history are statistically independent.

Another key aspect for getting an adequate stochastic crack-growth model is to accurately consider the statistical correlation between the estimation of the fatigue-model parameter. For example, for a Paris-law model for Virkler data shown in Figure 28.12, the absolute value of statistical correlation coefficient between

the estimate of the model coefficient and the estimate of the model exponent is as high as 0.90. Assuming statistical independence between the two random parameters of the Paris-law model produces significant modeling error that can affect the computed fatigue-failure risks by an order of magnitude.

28.3.2 Corrosion Damage

Corrosion in aluminum alloys can be broadly characterized into three types: pitting, general, and intergranular [47, 48]. The development of corrosion and its subsequent growth is less well described than is fatigue.

Pitting is a form of localized corrosion that takes the form of cavities on the surface of a metal. Pitting starts with the local breakdown of protective surface films. Pitting may cause the perforation of thin sections, as well as creating stress concentrations that may trigger the onset of fatigue cracking or other types of corrosion. Simplistic models for the progression of pitting corrosion are widely available.

Corrosion of aluminum alloys generally starts with pitting. Isolated pits are difficult to detect, but they have a significant effect on the fatigue life. Pits can occur on boldly exposed surfaces or on the faying surfaces of joints. Pits are stress concentrations where cracks can form; deep, narrow pits are essentially cracks. Even mild levels of pitting can significantly decrease the fatigue life of laboratory specimens. As pitting becomes widespread, a large area of material can become thinner, resulting in higher stress in that location. This increase in stress is generally less than the stress concentration at an isolated pit, but it is over a larger volume of material than with an isolated pit. These thinned regions will cause long cracks to grow faster, while pits will cause cracks to nucleate faster.

General corrosion is when pitting becomes so widespread that individual pits can no longer be identified. As a result, a significant area of the structure becomes thinner, resulting in higher stress at that location. This increase in stress is generally less than the stress concentration at an isolated pit, but it is over a larger volume of material than with an isolated pit. As a result, unless the structure is lightly loaded or used infrequently, cracking due to the interaction of fatigue and corrosion occurs well before general corrosion develops. If general corrosion occurs within a joint, the trapped corrosion products may cause bulging in the joint. Models for how general corrosion progresses are not readily available.

Intergranular corrosion develops out of pits as a result of preferential attack of the grain boundaries, as shown in Figure 28.16 [49]. Exfoliation and stress corrosion cracking (SCC) are special types of

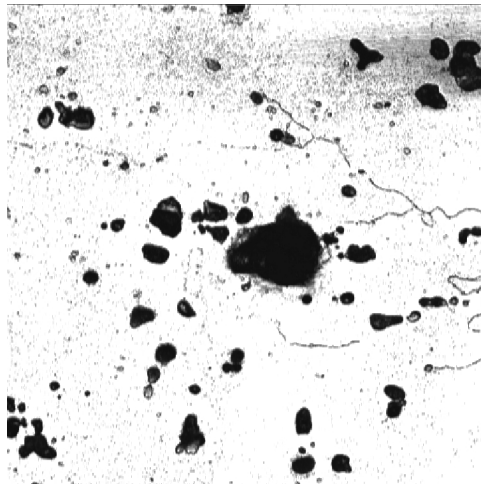


FIGURE 28.16 Photomicrograph of pits with intergranular corrosion on surface of 2024-T3 sheet (4 mm thick) after 4 h of exposure to 3.5% NaCl solution with no load applied (specimen PG-11). (From Bell, R.P., Huang, J.T., and Shelton, D., Corrosion Fatigue Structural Demonstration Program, Lockheed-Martin final report for AFRL/VASM, 2004, [49]. With permission.)

intergranular corrosion that occur in materials with directional grain structures (exfoliation) or under the influence of sustained tensile loads (SCC). The growth of intergranular corrosion is highly dependent upon chemical and metallurgical conditions and is not easily predicted.

28.3.2.1 Corrosion Pitting

In this subsection, two of the most accepted pitting models are described.

28.3.2.1.1 Power-Law Pit Model

For a boldly exposed surface, the depth of the deepest pit, a , as a function of exposure time, t , is typically described by a power law [50],

$$a = At^{1/n} \quad (28.19)$$

where A and n are empirically determined parameters, with n usually having a value between 2 and 4. This relationship does not mean that any one pit grows at this rate. Pits develop, sometimes rapidly, stagnate, and new pits begin. Rather, this equation represents how the maximum of the distribution of pit depth changes with time. An example of laboratory pitting data for 2024-T3 sheet in 3.5% NaCl solution is shown in Figure 28.17. The least-squares fit of the power-law equation to the data results in n equal to 2.52 and A equal to $20.07 \mu\text{m}$. These pit depths were measured with either an optical microscope or a confocal microscope from the surface of the specimen. If the pit tunneled, as in Figure 28.18, this could not be determined until after the specimen was broken open.

28.3.2.1.2 Wei Pit Model

A spatial pit-growth model was proposed by Wei [51, 52]. This pit-growth model assumes that the pit shape is a hemispherical shape and that its size grows at a constant volumetric rate, dV/dt , given by

$$\frac{dV}{dt} = 2\pi a^2 \frac{da}{dt} = \frac{MI_{p0}}{nF\rho} \exp\left(-\frac{\Delta H}{RT}\right) \quad (28.20)$$

By integrating the above equation, the pit depth a at a given time t is given by

$$a = \left\{ \left[\frac{3MI_{p0}}{2\pi nF\rho} \exp\left(-\frac{\Delta H}{RT}\right) \right] t + a_0^3 \right\}^{1/3} \quad (28.21)$$

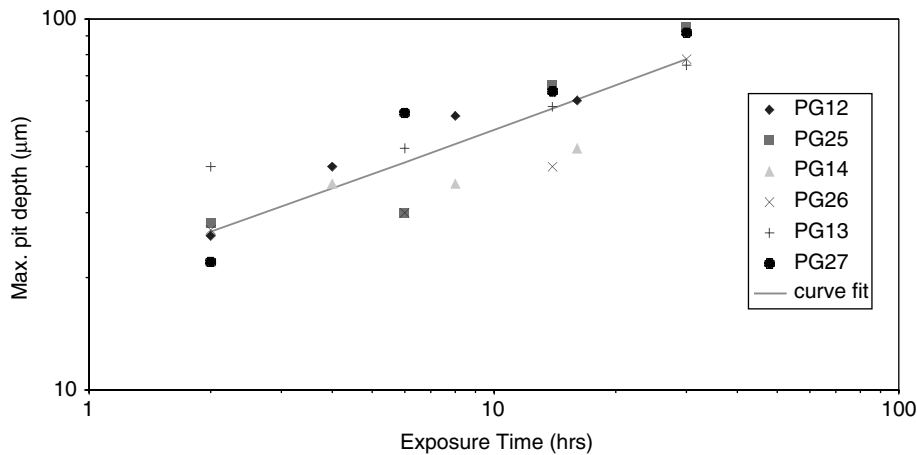


FIGURE 28.17 Maximum pit depth vs. time in 3.5% NaCl solution for 2024-T3 sheet (1.6 mm thick). (From Bell, R.P., Huang, J.T., and Shelton, D., Corrosion Fatigue Structural Demonstration Program, Lockheed-Martin final report for AFRL/VASM, 2004, [49]. With permission.)

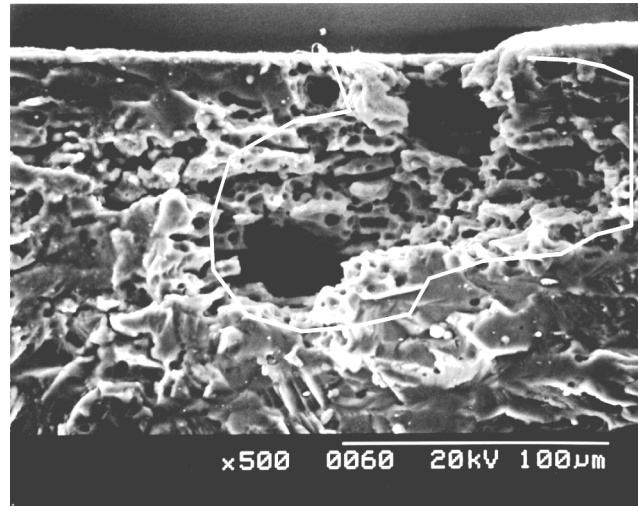


FIGURE 28.18 Example of pit that tunneled (specimen PG14). The pit is outlined by the white curve. (From Bell, R.P., Huang, J.T., and Shelton, D., Corrosion Fatigue Structural Demonstration Program, [51]. With permission.)

where a_0 is the initial pit radius, M is the molecular weight of the material, n is the valence, $F = 96,514$ C/mole is Faraday's constant, ρ is density of the material, ΔH is the activation energy, $R = 8.314$ J/mole-K is the universal gas constant, T is the absolute temperature, and I_{p0} is the pitting current coefficient.

In the Wei model, the assumption of a hemispherical shape of the pits introduces a significant modeling uncertainty. Pit shape is quite an important aspect. The pit depth alone does not adequately describe the stress concentration at a pit. Pit shapes are quite variable and can change with continuing corrosion. Pit shape is influenced by the microstructure of the material that developed as a result of prior thermomechanical processing, the environment (both mechanical and chemical), and the corrosion protection system. More-sophisticated models of pitting corrosion are clearly needed.

28.3.2.2 Stochastic Variability of Corrosion in Aluminum Alloys

28.3.2.2.1 Field Studies

Several long-term studies have been done to determine the statistical effects of environmental exposure on 2024-T3 aluminum materials [53, 54]. The first study [53] was conducted under the direction of the Atmospheric Exposure Test Subcommittee of ASTM Committee B-7 on Light Metals and Alloys. Several magnesium and aluminum alloys, including bare and clad 2024-T3 sheet (1.63 mm thick), were exposed at five test sites for periods of $1/2$, 1, 3, 5, and 10 years. The specimens included riveted joints as well as single-piece panels. The principal measurement in this test program was the change in tensile strength as a result of the exposure.

The second test program [54] involved four test sites for periods of 1, 2, and 7 years. The four test sites represented rural marine (Kure Beach), industrial marine (Corpus Christi, TX), moderate industrial (Richmond, VA), and industrial (McCook, IL). In this test program, pit depths, mass loss, and changes in tensile strength were recorded. A plot of maximum pit depth vs. exposure time is presented in Figure 28.19. The results indicate that while corrosion in a seacoast environment may start more quickly, there is not much additional corrosion with continued exposure. After 7 years, all the panels have about the same maximum pit depth. The corrosion rate at each of the locations was determined from the total mass loss per unit area divided by the total days of exposure and reported as milligrams lost per square decimeter per day, mdd (Figure 28.20). It is interesting to note that while the marine environments initially had deeper pits than the industrial environments, the industrial environments had higher corrosion rates. The locations with higher

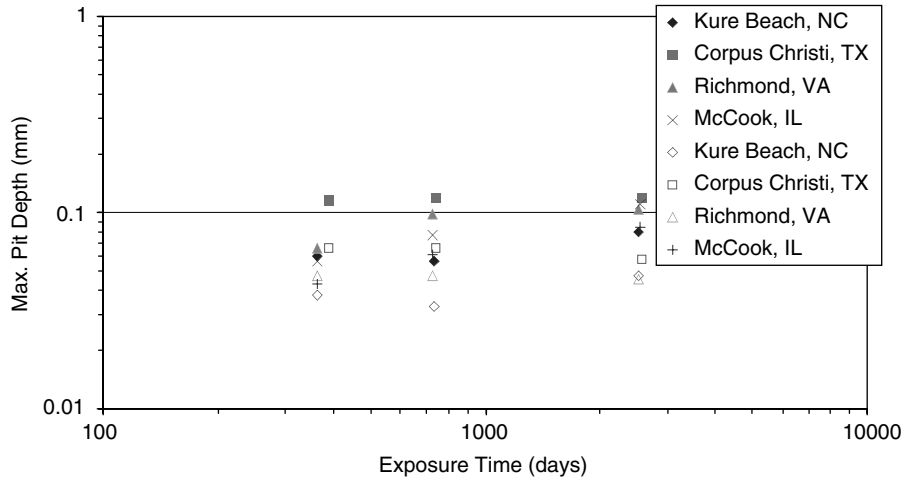


FIGURE 28.19 Maximum pit depths on exposed 2024-T3 sheet (1.63 mm thick). (Solid symbols are maximum depths; open symbols represent average of the deepest four pits.) (From Ailor, W.H., Jr., Performance of aluminum alloys at other test sites, in *Metal Corrosion in the Atmosphere*, ASTM STP 435, ASTM, 1968, pp. 285–307. With permission.)

corrosion rates likely had more pits per unit area, or there was more tunneling of the pits. These corrosion rates are for “boldly” exposed material.

In practical applications, the goal of a stochastic corrosion model is to obtain either the distribution of corrosion damage at any service time or the distribution of service times to reach any given level of corrosion. Different distributions may be required for corrosion on exposed surfaces and for corrosion in occluded areas such as joints. However, data on corrosion in occluded areas is just now becoming available.

28.3.2.2.2 Laboratory Studies

Numerous laboratory studies with accelerated protocols have looked at the distribution of corrosion pit sizes [55–57]. Pitting on exposed surfaces is primarily a function of the dispersion of constituent

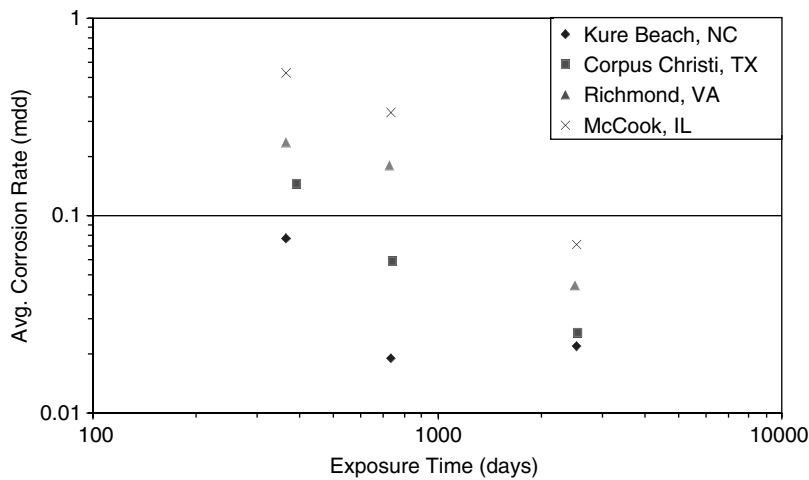


FIGURE 28.20 Corrosion rates for 2024-T3 sheet (1.63 mm thick) at four sites. (From Ailor, W.H., Jr., Performance of aluminum alloys at other test sites, in *Metal Corrosion in the Atmosphere*, ASTM STP 435, ASTM, 1968, pp. 285–307. With permission.)

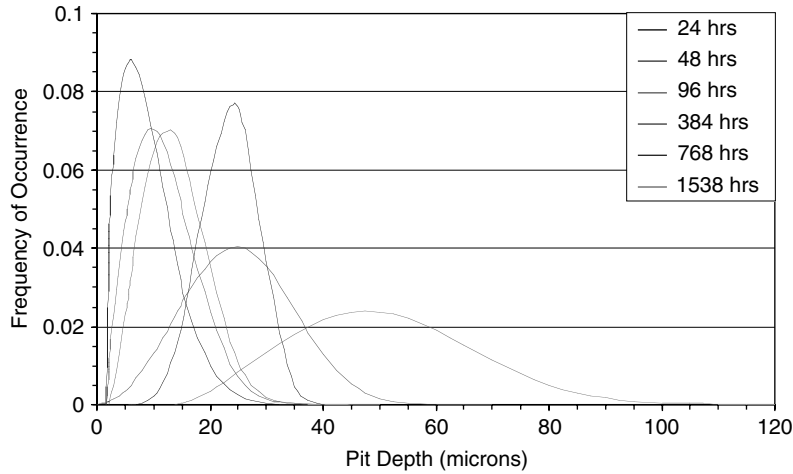


FIGURE 28.21 Three-parameter Weibull distributions of pit depth as a function of exposure time for 7075-T6.

particles in the material microstructure and not the environment. The stochastic descriptions of pitting developed during accelerated laboratory programs should be applicable to pitting on exposed surfaces in natural environments.

Sankaran et al. [55] estimated the distributions of pit dimensions on 7075-T6 as a function of time exposed per ASTM G85 Annex 2 from 200 randomly selected pits at each exposure time (Figure 28.21, Figure 28.22, Figure 28.23). The progression of these distributions with time exhibited a ratcheting behavior. This can be seen in the sequence of pit-depth distributions from 96-h exposure to 1538-h exposure shown in Figure 28.21.

In the studies of pitting on 2024-T3 [56, 57], statistics are reported on the projected area of the pits perpendicular to the loading direction. The Gumbel extreme-value distribution was used to describe the projected areas of the largest pits (Figure 28.24). Note that the area of these pits at 192 h of exposure is an order of magnitude greater than was the area of the pits in the 7075-T6 tests [55].

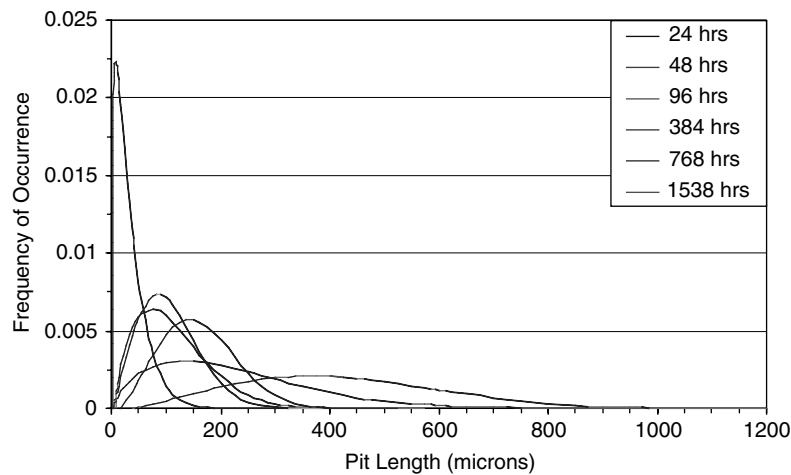


FIGURE 28.22 Three-parameter Weibull distributions of pit length (in rolling direction of sheet) as a function of exposure time for 7075-T6.

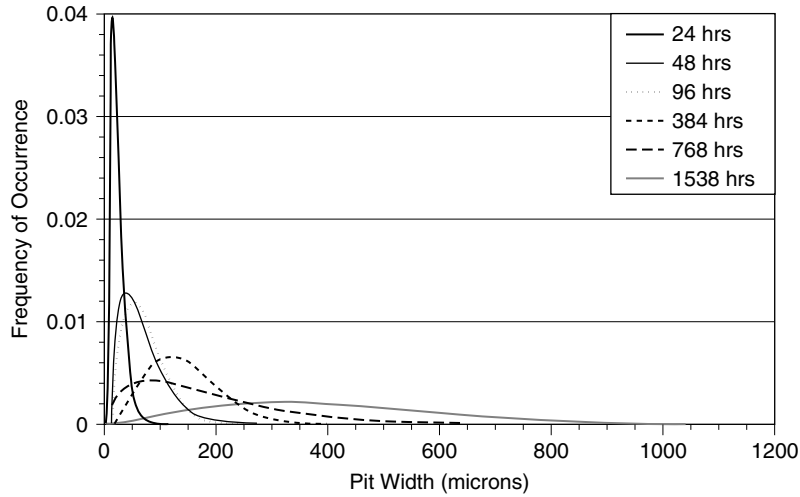


FIGURE 28.23 3-Parameter Weibull distributions of PitWidth (perpendicular to rolling direction of sheet) as function of exposure time for 7075-T6.

This is probably the result of the different severities of the environments and not any inherent material characteristics.

In subsequent fatigue analyses, the pits in the 2024-T3 materials were treated as semicircular surface cracks with a depth-to-width ratio of 0.5 and of equivalent area, which is the most severe case for these small “cracks.” Data from the 7075-T6 tests demonstrate that a constant depth-to-width ratio is not realistic, as illustrated by the Weibull distributions shown in Figure 28.25. The nonanalytical estimated bivariate joint probability distribution of pit depth size and pit width is plotted in Figure 28.26. Engineering experience shows that the impact of ignoring the pit aspect ratio in fatigue-crack growth analyses is to potentially overestimate the stress intensity by about a factor of 2, which could lead to overestimating the crack growth rate by an order of magnitude or even more.

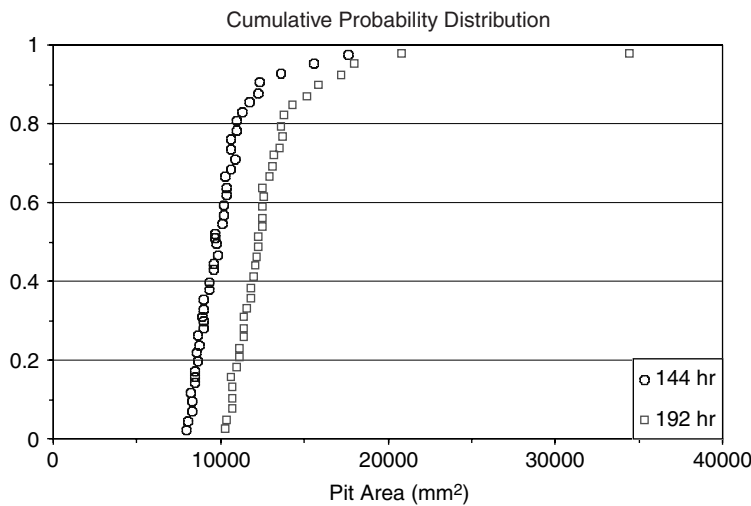


FIGURE 28.24 Extreme-value plots of pit area for largest 10% pits in 2024-T3 material. LT plane exposed to 3.5% salt water in alternate immersion for 144 h and 192 h. Pit area measured on ST plane.

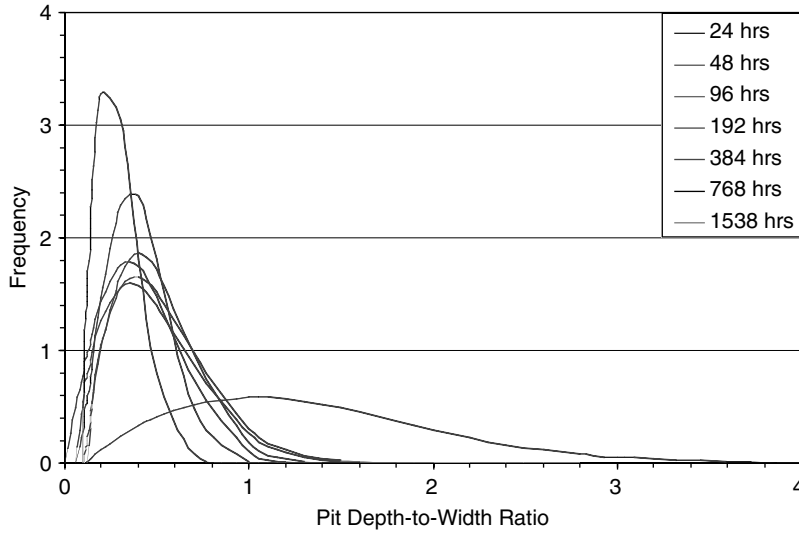


FIGURE 28.25 Three-parameter Weibull distribution of the pit depth-to-width ratio as a function of exposure time for 7075-T6.

28.3.2.2.3 Corroded Surface Topography

Corroded surface topography can have significant influence on corrosion progression and fatigue resistance due to its influence on the local stresses and stress intensity factors. Corroded surface topography incorporates all the key stochastic aspects of the random corrosion progression. At a global scale, in an average sense, the corrosion topography is defined by the general thickness loss, while at a local scale the corrosion topography is defined by the pitting geometry. The corrosion starts as pits on the surface at the boundaries between the aluminum matrix and constituent particles, and then grows with a rough spatial profile due to highly variable growth rates for individual pits. Finally the surface becomes slightly smoother as the pits broaden and link up to form a general corroded surface. Data on

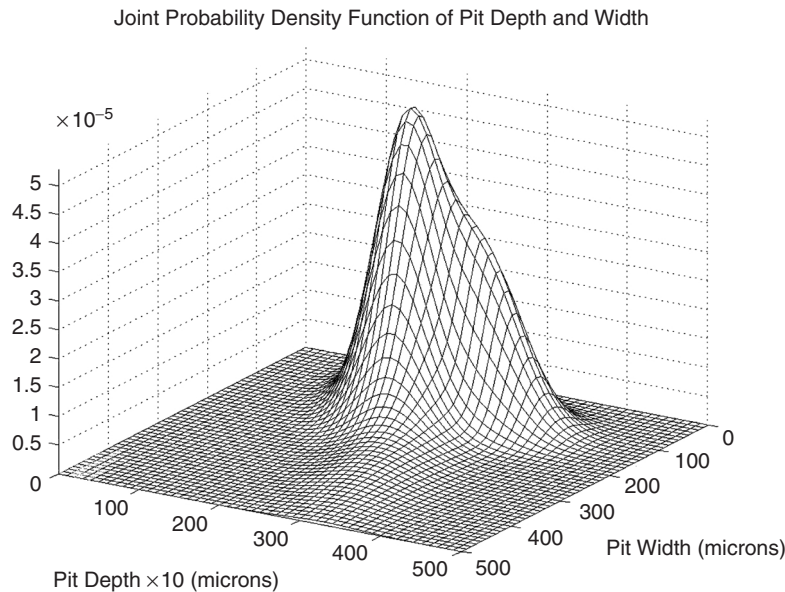


FIGURE 28.26 Joint PDF of pit depth and width after 768 h.

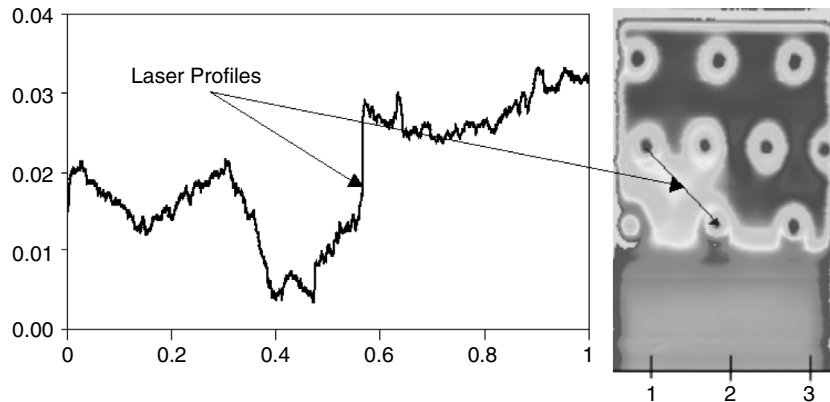


FIGURE 28.27 Thickness map of corroded surface and fine-detail line scan.

the time progression of corroded surfaces through these phases is lacking. Corrosion topography influences both the local stresses (through local pitting) and far-field stresses (through general thickness loss). A typical corroded surface and a cut-line (laser) profile through it is shown in Figure 28.27. Mathematically, stochastic corrosion surfaces can be handled using stochastic field-expansion models such as proper orthogonal decomposition or Karhunen-Loeve series expansion [58, 59].

28.3.3 Corrosion-Fatigue Damage

In this section the effects of corrosion of both crack initiation and propagation stages are discussed. Then, three corrosion-fatigue damage models are presented. These models are the Wei corrosion-fatigue (WCF) model [53, 54], the crack-closure corrosion-fatigue (CCCF) model [42], and the simultaneous corrosion-fatigue (SCF) model [8]. The WCF model replaces the crack-initiation model with a corrosion-pitting model, and after a crack is initiated, the corrosion has no effect on the fatigue cracking. The CCCF and SCF models incorporate the corrosion effects on fatigue cracking during both the crack-initiation and the crack-propagation stages.

Corrosion effects are of two kinds: (1) a local increase in stress near a corrosion pit and (2) a general increase of the far-field stress due to component thickness loss. Pitting can dramatically reduce component life, but it is only significant during the crack initiation phase. General thickness loss has a less dramatic effect on the time to form a crack, but the increased stress can speed up the growth of existing cracks.

Pitting corrosion usually shortens the time for cracks to form, in some cases eliminating the crack nucleation phase altogether. The reduction in the nucleation portion depends on the amount of corrosion, which in turn depends upon the length of exposure to the corrosive environment and the severity of the corrosive environment in relation to the rate at which load cycles are applied. It is difficult to simulate the effect of natural environments in the laboratory because of the time scale involved (20 to 30 years), and currently the relationship between the time scales in accelerated corrosion tests to the natural environment has not been established. So synchronizing the rate at which load cycles are applied with corrosion rate is impossible.

In the laboratory, cracks grow faster in aggressive environments. It is not clear how significant the environmental effects on crack growth are for aircraft structures. Many of the fatigue loads are applied when the aircraft is flying high, where conditions are cold and relatively dry. There can be condensation of moisture inside a transport aircraft. This creates at most a humid environment, so crack growth in humid air may be appropriate. Takeoff and landing loads can be applied in a warm and humid external environment, but this is a small fraction of each flight, unless the aircraft is used for short hops. Recent data gathered from coupons mounted in the wheel wells and vertical tails indicate that most corrosion

in USAF transport aircraft occur while the aircraft is on the ground [60]. In general, crack growth rates in high-humidity air should be used for crack-propagation assessments on USAF aircraft.

Local corrosion, such as pitting, on the surface of a part does not greatly affect the growth of long cracks. Because the crack is “sampling” through the thickness of the material, small stress fluctuations at the surface affect only a small local portion of the crack. Not until corrosion becomes so widespread that there is a general loss of part thickness is crack growth affected. Then the crack growth rate increases because stress increases in the part.

28.3.3.1 Wei Corrosion-Fatigue (WCF) Model

The Wei model was developed over a period of several years [51, 52]. As described above, the Wei models assume two stages of corrosion-fatigue damage growth. The first stage is the corrosion stage due to initial pitting, which continues until a threshold level is reached (threshold corresponds to an equal growth rate of pit depth and crack depth, after which crack growth takes over). The second stage is the fatigue stage that ends with the material failure. The Wei models include two fatigue-crack stages, a surface-crack stage and then a through-crack stage. The surface-crack-fatigue part of the Wei models is based on simple Paris-law, with a ΔK_{th} of $3 \text{ MPa}\sqrt{\text{m}}$ for 2024-T3 aluminum. Thus, in the Wei model, corrosion is just the initiator of fatigue damage due to crack growth. After fatigue takes over (crack-depth growth rate is larger than pit-depth growth rate), corrosion has no further effect. This is a different concept than the SCF model that is presented in this section.

The time to failure, t_f is given by

$$t_f = t_{ci} + t_{tc} + t_{cg} \quad (28.22)$$

where, t_{ci} is the time required for a nucleated pit to grow and for a surface crack to initiate from it, t_{tc} is the time required for the surface crack to grow into a through crack, and t_{cg} is the time for a through crack to grow to a prescribed critical length, given as a part of a failure criterion.

Using the pit-growth equation given by Wei, the time for the pit to grow to a_{ci} is given by

$$t_{ci} = \frac{2\pi n F \rho}{3 M I_{p0}} (a_{ci}^3 - a_0^3) \exp\left(\frac{\Delta H}{RT}\right) \quad (28.23)$$

The pit radius at which a crack is initiated, a_{ci} , can be expressed in terms of the threshold driving force ΔK_{th} via crack growth mechanism. For the sake of simplicity and computational expediency, the surface crack remains semicircular in shape, and the stress-intensity-factor range is given by

$$\Delta K_s = \frac{2.2}{\pi} K_t \Delta \sigma \sqrt{\pi a} \quad (28.24)$$

where $\Delta \sigma$ is the far-field stress range, K_t is the stress concentration factor resulting from the circular rivet hole, and the factor of $2.2/\pi$ is for a semicircular flaw in an infinite plate. Again, the surface crack is assumed to nucleate from a hemispherical corrosion pit when ΔK_s increases to ΔK_{th} . The corresponding crack length that satisfies this condition is easily found to be

$$a_{ci} = \pi \left(\frac{\Delta K_{th}}{2.2 K_t \Delta \sigma} \right)^2 \quad (28.25)$$

The expression for t_{ci} can be found by substituting Equation 28.25 into Equation 28.26. The material parameters of the Wei corrosion model for 2024-T3 aluminum are shown in Table 28.6.

Within the Wei corrosion-fatigue model, a standard Paris law is assumed for crack propagation:

$$\left(\frac{da}{dN} \right)_c = C_c (\Delta K)^n \quad (28.26)$$

TABLE 28.6 Parameters Used in the Pit-Growth Model for 2024-T3

Parameters	2024-T3	Parameters	2024-T3
Density, ρ (gm/m ³)	2.7×10^6	Initial pit radius, a_0 (m)	2×10^{-5}
Molecular weight, M	27	Pitting current constant, I_{p0} (C/sec)	0.5
Valence, n	3	Threshold, ΔK_{th} (MPa \sqrt{m})	3.0
Activation energy, ΔH (J/mole)	50,000	Applied stress, $\Delta\sigma$ (MPa)	90
Temperature, T (K $^\circ$)	293	Stress concentration factor, K_t	2.6

The driving force ΔK is considered to be of two different forms, according to whether the crack is a surface crack or a through crack. For a surface crack, ΔK equals ΔK_s given in Equation 28.24, and it remains so until the crack can be modeled as a through crack. When the crack becomes a through crack, ΔK is assumed to be equal to ΔK_{tc} , which has the following form:

$$\Delta K_{tc} = F_{tc} \left(\frac{a}{r_0} \right) \Delta\sigma \sqrt{\pi a} \quad (28.27)$$

where r_0 is the radius of the rivet hole. For ratios of a/r_0 in the interval from 0 to 10, inclusive, for an infinite plate under uniaxial tension containing a circular hole with a single through crack emanating from the hole perpendicular to the loading axis, the function $F_{tc}(a/r_0)$ can be numerically evaluated by

$$F_{tc} \left(\frac{a}{r_0} \right) = \frac{0.865}{(a/r_0) + 0.324} + 0.681 \quad (28.28)$$

The remaining question concerning the driving force ΔK is that of the transition from a surface crack to a through crack. It is assumed that the transition occurs at the crack length a_{tc} , which is defined by equating the geometry-dependent function from Equation 28.24 and Equation 28.28. Thus, the transition crack length a_{tc} is the solution of

$$F_{tc} \left(\frac{a_{tc}}{r_0} \right) = \frac{2.2}{\pi} K_t \quad (28.29)$$

which is easily found to be

$$a_{tc} = r_0 \left[\frac{0.865}{(2.2/\pi)K_t - 0.681} - 0.324 \right] \quad (28.30)$$

The final computation to be completed is for t_{tc} and t_{cg} . First consider the computation for the time between crack initiation and transition to a through crack, t_{tc} . Substituting Equation 28.24 into Equation 28.26 yields a simple differential equation in that the variables a and N can be separated, and an explicit solution can be found. Assuming that $N = \nu t$, where ν is the loading frequency, then

$$t_{tc} = \frac{2(\sqrt{\pi})^{n_c} [(\sqrt{a_{tc}})^{2-n_c} - (\sqrt{a_i})^{2-n_c}]}{\nu(n_c - 2)C_c(2.2K_t\Delta\sigma)^{n_c}} \quad (28.31)$$

if $n_c \neq 2$. For aluminum alloys, typically n_c is not equal to 2.

The time between the through-crack initiation time and the final failure time is

$$t_{cg} = \int_{a_{tc}}^{a_f} \frac{1}{\nu C_c (\Delta\sigma \sqrt{\pi})^{n_c}} \left(\frac{0.324r_0 + a}{1.086r_0 \sqrt{a} + 0.681(\sqrt{a})^3} \right)^{n_c} da \quad (28.32)$$

TABLE 28.7 Parameters Used in the Crack Growth Model for 2024-T3

Parameters	2024-T3	Parameters	2024-T3
Fatigue coefficient, C_c (m/cycle)	3.3×10^{-10}	Final crack size, a_f (mm)	3.0
Crack growth exponent, n_c	3.0	Frequency, ν (cycles/day)	2, 10
Radius of rivet hole, r_0 (mm)	3.0	Threshold, ΔK_{th} (MPa \sqrt{m})	3.0

Source: Ailor, W.H., Jr., Performance of aluminum alloys at other test sites, in *Metal Corrosion in the Atmosphere*, ASTM STP 435, ASTM, 1968, pp. 285–307.

where a_f is the final crack size. In most cases, the t_{cg} can only be calculated by numerical integration. The parameters for crack growth that are shown in Table 28.7 are from the literature [52].

28.3.3.2 Crack-Closure Corrosion-Fatigue (CCCF) Model

The crack-closure fatigue model [42] was modified to include the effect of corrosion pitting on the local stress intensity. To include corrosion pit effects the effective-stress-intensity range, ΔK_{eff} , is amplified by a pitting factor as follows:

$$\Delta K'_{eff} = \psi(t) \Delta K_{eff} \quad (28.33)$$

The pitting factor $\psi(t)$ depends on pit size and crack size:

$$\psi(t) = \sqrt{1 + \frac{a_{pit}(t)}{a_{crack}(t)}} \quad (28.34)$$

Equation 28.33 and Equation 28.34 are equivalent to an additive corrosion-fatigue-damage model that superimposes linearly the corrosion damage, pit size, fatigue damage, and crack size in the stress-intensity analytical expression. Since, practically, there is no corrosion during flights, only the ground time is considered for evaluating the corrosion pit growth. The pit growth, Equation 28.34, is computed using Wei pit model Equation 28.21.

28.3.3.3 Simultaneous Corrosion-Fatigue (SCF) Model

The SCF model describes corrosion-fatigue damage occurring simultaneously [8]:

1. Cracks form during the crack nucleation phase. The time to form a crack can be decreased by corrosion that occurs during the crack nucleation phase.
2. Cyclic loading is interspersed with periods of pit growth, which increases the local stress concentration factor.
3. If load cycles are applied infrequently, pitting may transition to general corrosion and thickness loss, leading to an increase in the global stress.
4. Once a crack is formed, only the thickness loss due to general corrosion and the associated stress increase affect the growth rate of the crack.

The SCF model is implemented as follows: (1) for crack initiation, an additive incremental total damage model that linearly superimposes the pit-depth increment and the stress-concentration factor, and (2) for crack propagation, two time-variant corrosion-topography factors (pitting and thickness loss factors) that multiply the stress-intensity-factor range.

28.3.3.4 Comparative Results

In this subsection, computed results obtained using the deterministic corrosion-fatigue models described above are compared.

Figure 28.28 and Figure 28.29 compare the WCF model and the CCCF model for a plate with a hole [51]. The plate is 90 mm wide and 1.3 mm thick. The hole has a 3-mm radius and is located in the center of the plate. The initial pit size, corresponding to the size of the constituent particle from which

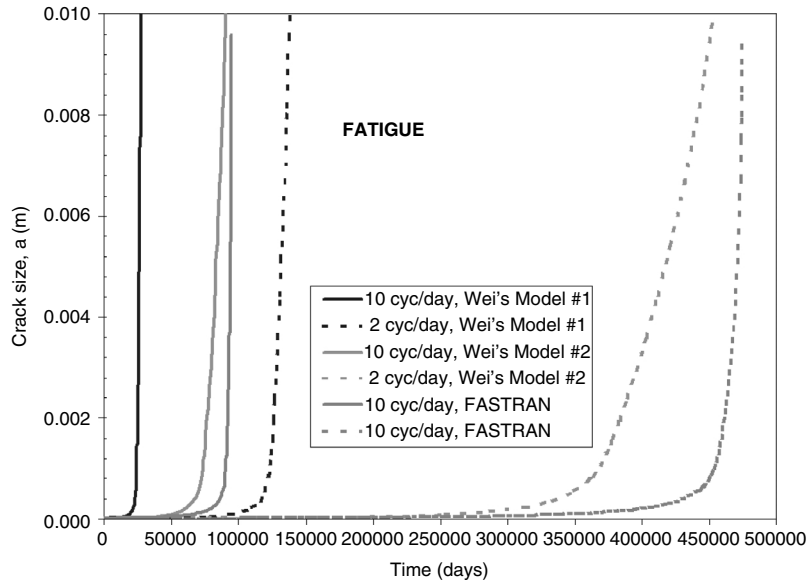


FIGURE 28.28 Results of the WCF and CCCF model (using FASTRAN) for pure fatigue.

the pit starts, is $20\ \mu\text{m}$. The constituent particle shape was assumed to be hemispherical. Two aircraft operating scenarios are considered here: (1) 10 load cycles/day, assuming 15-h flight and a 9-h stay on ground (for same location); and (2) 2 load cycles/day, assuming 3-h flight and 21-h stay on ground (for same location). The stress range was 90 MPa at temperature, and the notch factor was $K_t = 2.6$. The material was 2024-T3 aluminum. The fatigue coefficient, C_s , and the exponent, n_s , were assumed to be $3.95\ \text{E}-11$ and 3.55 for Wei model 1 [52] and $1.86\ \text{E}-11$ and 3.15 for Wei model 2, respectively.

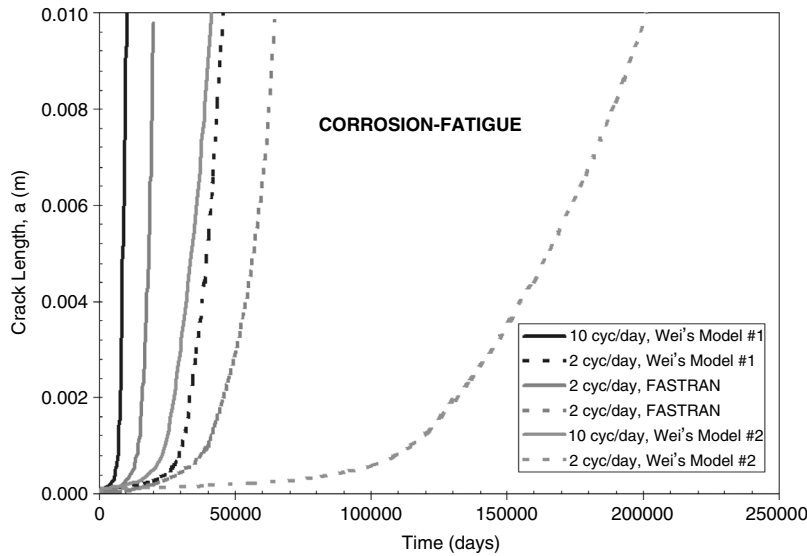


FIGURE 28.29 Results of WCF and CCCF model (using FASTRAN) for corrosion fatigue.

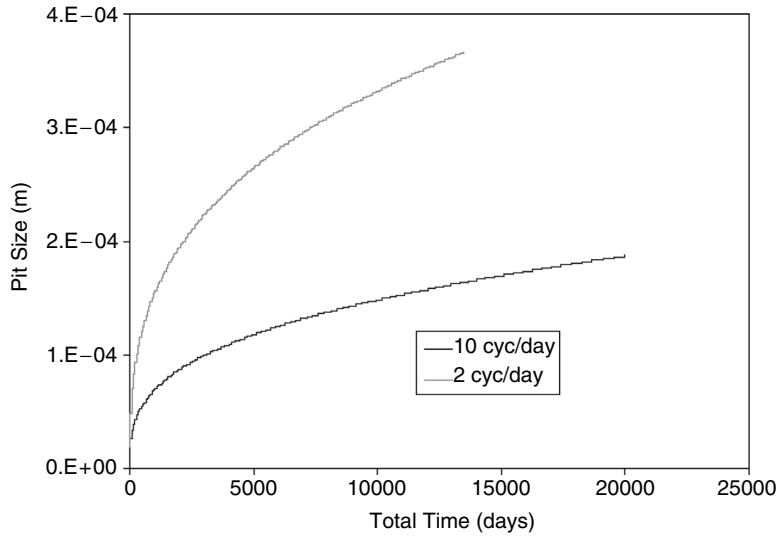


FIGURE 28.30 Pit-depth curves for the two operating scenarios for aircraft.

The pit-growth and the pitting-factor curves for the two corrosion scenarios are plotted in Figure 28.30 and Figure 28.31, respectively. The pit-growth curves are the same for the WCF and CCCF models. The pitting factors are applied only in conjunction with the CCCF model (Equation 28.33 and Equation 28.34).

Figure 28.28 shows the pure-fatigue lives computed for the WCF models and the CCCF model assuming 10 cycles/day and 2 cycles/day, respectively. Figure 28.29 shows the corrosion-fatigue lives using the same models. Only the time on ground was considered for corrosion growth. The computed lives are also included in Table 28.8.

It should be noted from Figure 28.28, Figure 28.29 and Table 28.8 that the range of results of the WCF model 1 and model 2 include the CCCF results. For pure fatigue, there is a poor matching between the lives computed using Wei model 1 and CCCF. The Wei model 2 matches quite well the FASTRAN results

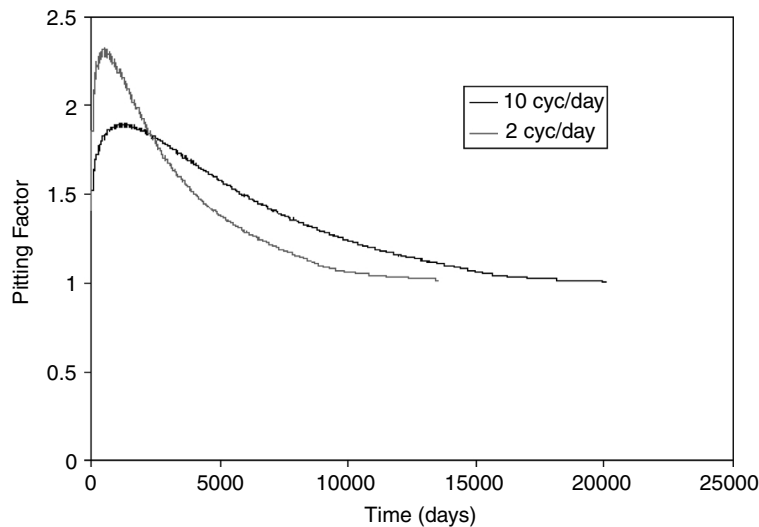


FIGURE 28.31 Pitting corrosion factor for the two operating scenarios for aircraft.

TABLE 28.8 Comparative Life Results Using WCF Models and CCCF Model

Investigated Case	WCF- Wei Model 1	WCF-Wei Model 2	CCCF
Fatigue, 10 cycles/day	27,560 days	90,647 days	94,905 days
Fatigue, 2 cycles/day	137,802 days	453,239 days	474,850 days
Corrosion fatigue, 10 cycles/day	10,185 days	41,320 days	20,018 days
Corrosion fatigue, 2 cycles/day	45,370 days	201,046 days	64,951 days

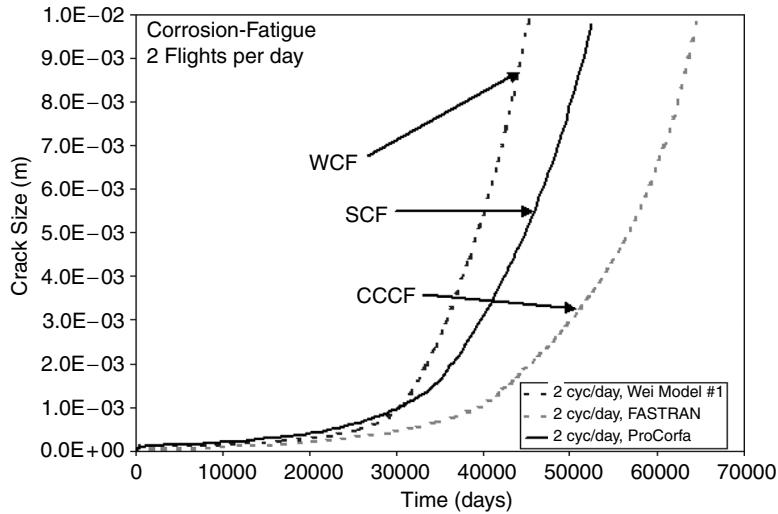


FIGURE 28.32 Comparative life predictions for 2 cycles/day using WCF model, SCF model, and CCCF model.

for pure fatigue, while the Wei model 1 agrees better than the Wei model 2 with CCCF results for the largest corrosion damage, namely, the 2-cycles/day case (21 h/day stay on ground).

Figure 28.32 and Figure 28.33 compare the WCF, CCCF, and SCF models for the two previous corrosion-fatigue scenarios. In this comparison, the SCF model uses the LDR for crack initiation combined with the

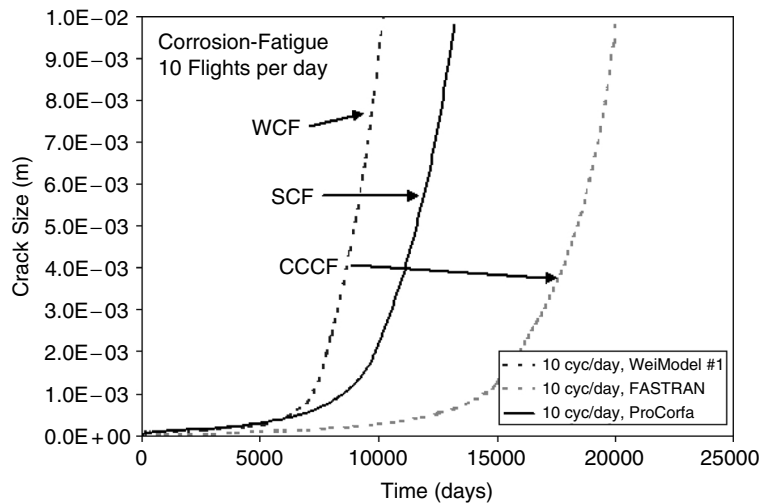


FIGURE 28.33 Comparative life predictions for 10 cycles/day using WCF model, SCF model, and CCCF model.

Forman model for crack propagation (Table 28.3 and Table 28.4). The main difference between the WCF model results and the SCF model results are due to the different fatigue-crack-propagation models used. WCF uses a truncated Paris-law model, and SCF uses the Forman model. The crack growth threshold, ΔK_{th} , was taken equal to $3 \text{ MPa}\sqrt{\text{m}}$. The Paris-law model was truncated at this threshold value.

28.4 Reliability of Aircraft Structure Joints Including Maintenance Activities

The reliability analysis concept is illustrated in Figure 28.34. It can be seen in the figure that the effect of corrosion on fatigue life is to increase the time-variant failure risk and to produce unscheduled maintenance events. In Figure 28.34, notation SME stands for scheduled maintenance events, and notation UME stands for unscheduled maintenance events. In the figure, the probability distributions of the crack size population before and after the inspections are also shown. The result of inspection is the replacement (or repair) of the components with larger cracks, which are most likely to be detected by inspections.

28.4.1 Risk/Reliability-Based Condition Assessment

Component risk/reliability-based condition assessment is usually based on three risk/reliability metrics: (1) instantaneous probabilistic failure risk that expresses the risk at any given time or damage level, (2) component remaining life (when no maintenance activity is included), and (3) future probabilistic failure risk that expresses the risk in the next time interval (this future interval is associated with a maintenance interval).

28.4.1.1 Physics-Based Reliability Engineering Approach

The physics-based reliability engineering approach integrates the structural reliability theory with the reliability engineering theory. The basic relationship that links the two theories is the relationship between

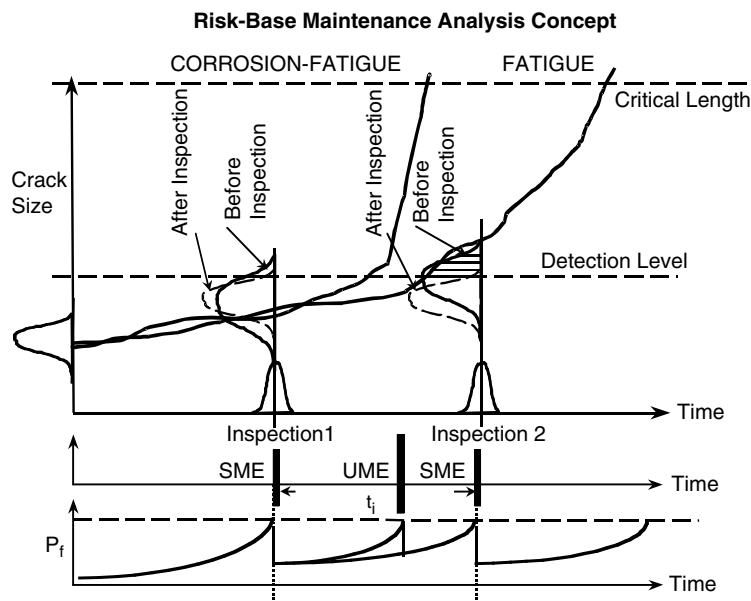


FIGURE 28.34 Risk/reliability-based maintenance analysis concept.

the computed instantaneous failure probability and the hazard failure rate at any given time:

$$\text{Prob}[T_f \leq t + \Delta t | T_f > t] = P_f(t) + [1 - P_f(t)] \exp \left[- \int_t^{t+\Delta t} h(x) dx \right] \quad (28.35)$$

The above equation expresses the failure probability within a time interval that defines the probability distribution of a component life, in terms of the instantaneous failure probability computed at the starting time of the interval, $P_f(t)$, and the variation of the hazard failure rate, $h(x)$, in the interval. Then, the reliability engineering metrics, such as MTBF (mean time between failures) that are required for maintenance cost analysis can be computed by integrating the reliability function (defined by unity minus the failure probability):

$$\text{MTBF} = \int_0^{\infty} [1 - P_f(t)] dt \quad (28.36)$$

Statistics and reliability metrics that are of interest to engineers and decision makers are:

1. Crack-length statistics evolution with no or multiple inspection intervals
2. Failure risk evolution with no or multiple inspection intervals
3. Reliability index evolution with no or multiple inspection intervals
4. Hazard failure rate evolution with no or multiple inspection intervals
5. Average hazard failure rates per inspection intervals
6. Number of failures (removals) per inspection intervals
7. PDF of the parent crack length population after each inspection
8. Equivalent Weibull failure (life) models
9. Posterior probability density function of life via Bayesian updating to incorporate failure data
10. Posterior PDF of crack size via Bayesian updating to include inspection data

An adequate risk/reliability-based condition assessment of an aircraft component with corrosion-fatigue damage needs to include the following analysis and modeling steps:

1. Stochastic modeling of operational loading condition and environmental conditions
2. Stochastic modeling of component loading, environmental surface conditions, and material and structural properties (This step may also include modeling of the component surface boundary conditions, such as contact-surface constraint effects, material property variations, manufacturing deviations from the baseline geometry, etc. These last aspects are not discussed here.)
3. Stochastic component stress/strain analysis to compute the stress/strain state in the component for given operating conditions that are time dependent
4. Stochastic modeling of component stress and strain histories at critical locations (This step includes the construction of principal-, component-, and equivalent-stress histories.)
5. Component reliability analysis or risk analysis for initial no-usage conditions (no deterioration due to progressive damage mechanisms) (This initial risk is due to stochastic variations in component design parameters, including manufacturing geometry deviations, material fabrication defects, assembly errors, etc. This time-invariant reliability problem is not discussed here.)
6. Reliability/risk-based condition assessment and life prediction (effect of maintenance is not included) based on stochastic damage models for both the crack-nucleation and crack-propagation stage
7. Reliability/risk-based maintenance analysis, including the effects of maintenance uncertainties on present failure risks, defined instantaneous failure risks, and future failure risks during the some time interval, typically selected to be the next inspection interval
8. Optimal-cost reliability/risk-based maintenance cost analysis, including the computation of overall maintenance costs vs. the component removal time based on reliability analysis results accounting for both scheduled maintenance events (SME) and unscheduled maintenance events (UME). (These postreliability analysis aspects are not discussed here.)

Two reliability analysis options are possible: (1) for a defined maintenance schedule and inspection techniques, the time-variant component risk/reliability (and unscheduled maintenance rates) can be computed, or (2) for a selected reliability level and selected inspection techniques, the required (scheduled) maintenance intervals can be determined.

28.4.1.2 Equivalent “Physics-Based” Weibull Failure Models

For practical purposes, equivalent Weibull component life models are determined based on the computational results of the physics-based reliability analysis. These equivalent “physics-based” Weibull life models have the advantage that they can be easily compared with the existing Weibull models developed from field failure data.

To compute the two parameters of the Weibull distribution, a least-squares error minimization technique is used to fit the random sample life data [61]. Before performing the least-squares fitting, a transformation of the coordinates is performed so that the Weibull distribution points are shown along a straight line.

For the equivalent Weibull model, the instantaneous failure probability is computed by

$$P_f(t) = 1 - e^{-\left(\frac{t}{\theta}\right)^\beta} \quad (28.37)$$

where β and θ are the shape and scale parameters of the Weibull distribution.

The Weibull hazard failure rate at time t is expressed by

$$h(t) = \frac{1}{\theta\beta\left(\frac{t}{\theta}\right)^{\beta-1}} \quad (28.38)$$

For a shape factor equal to unity, the Weibull distribution reduces to an exponential distribution that has a constant mean hazard failure rate.

28.4.1.3 Maintenance Inspection Uncertainties

To maintain an acceptable reliability level for a mechanical component, two strategies are available: (1) to design the component for a long life so that there is no need for any maintenance during service life, or (2) to allow maintenance through inspections during the component service life, with repairs as required. It is known that the second strategy corresponds to a more cost-effective approach and can help to extend the component service life. The key aspect for implementing such a strategy is to be able to accurately predict and control the evolution of the component’s failure risk, including all maintenance activities and their associated uncertainties.

28.4.1.3.1 Nondestructive Inspection (NDI) Techniques

Inspection routines are adopted to detect and remove cracks with sizes larger than a rejection limit, resulting in the improvement of reliability toward an acceptable level. For a particular NDI technique, several factors randomly affect the inspection results. For aircraft components, the most important influencing factors are those related to the precision of the type of NDI used and the operator skill.

The detection probability is defined as the number of times a crack of size “ a ” has been detected, divided by the number of trials, with each trial being performed by a different inspector or inspection team using the same inspection technique. Crack sizing errors include a significant statistical uncertainty. The literature includes some outstanding references on the subject [62–64].

The rejectable crack size a_R is also an important parameter for component maintenance. This limit size is specified based on safety and economic aspects. The rejectable crack size a_R (corresponding to repair or replacement) represents the limit for maintenance action on a detected crack of either accepting (leave) or rejecting (fix) it.

The rejectable crack size can be used to evaluate the following probabilities, where independence between additive sizing error and detection is assumed [62]:

1. The probability $P_R(a)$ of rejecting a crack with size a , calculated as the product of the detection probability and the probability of sizing the detected crack larger than a_R :

$$P_R(a) = P_D(a)[1 - F_S(a_R - a)] \quad (28.39)$$

2. The probability $P_A(a)$ of accepting a crack with size a , calculated as the product of the detection probability and the probability of sizing the detected crack smaller than a_R , added to nondetection probability:

$$P_A(a) = P_D(a)F_S(a_R - a) + [1 - P_D(a)] = 1 - P_R \quad (28.40)$$

In Equation 28.39 and Equation 28.40, F_S is the cumulative probability distribution of the statistical crack sizing errors. For a given crack size a , the sum of these two probabilities equals unity, since a crack must always be either rejected or accepted. For a particular case where $a > a_R$, the function $P_R(a)$ is called the probability of correct rejection, while for $a < a_R$, the function $P_A(a)$ is called the probability of correct acceptance. It should be observed that both $P_R(a)$ and $P_A(a)$ depend on the reliability of the inspection technique and on the specified rejection limit a_R . These definitions can be used to evaluate four additional parameters quantifying the global effect of an inspection procedure [62]:

1. The total probability of correctly rejecting a crack

$$P_{CR} = \int_{a_R}^{\infty} P_R(a)f_A(a)da \quad (28.41)$$

2. The total probability of incorrectly rejecting a crack

$$P_{IR} = \int_0^{a_R} P_R(a)f_A(a)da \quad (28.42)$$

3. The total probability of correctly accepting a crack

$$P_{CA} = \int_0^{a_R} P_A(a)f_A(a)da \quad (28.43)$$

4. The total probability of incorrectly accepting a crack

$$P_{IA} = \int_{a_R}^{\infty} P_A(a)f_A(a)da \quad (28.44)$$

Obviously, the sum of the above probabilities is unity, $P_{CR} + P_{IR} + P_{CA} + P_{IA} = 1$. The function $f_A(a)$ is the probability density function of the crack-length population before inspection.

28.4.1.3.2 Brief Description of NDE Inspection Types

Nondestructive evaluation (NDE) tests are used in maintenance to avoid loss of aircraft due to aging effects. They are also used in manufacturing to assure the quality of the components. Nearly every form of energy is used in nondestructive tests, including all wavelengths of the electromagnetic spectrum as well as mechanical vibration. These tests are divided into the following basic methods: visual, liquid penetrant, radiographic, ultrasonic, eddy-current, microwave, and infrared.

28.4.1.3.3 Probability of Detection (POD) Curves

The capabilities of NDE techniques are typically quantified by plotting the probability of detection (POD) as a function of flaw size. Berens and Hovey [65] have shown that a lognormal formulation for the POD

curve provides a reasonable model for the observed behavior of NDE data. The lognormal POD can be expressed as

$$\text{POD}(x) = \int_0^x \frac{1}{\sigma u \sqrt{2\pi}} \exp\left[-\frac{(\ln(u) - \mu)^2}{2\sigma^2}\right] du \quad (28.45)$$

Studies have been conducted by various organizations to determine POD curves for various NDE techniques when applied to various selected aircraft components. Similar to the POD curves for crack detection, POD curves for thickness loss due to corrosion can be determined. Figure 28.3 shows the POD curve for detecting thickness loss using an eddy-current NDE inspection of an unpainted 737 aircraft splice joint. It can be noticed from that figure that the operator's skill can significantly affect the POD curve for a given eddy-current NDE technology.

28.4.1.4 Probabilistic Modeling for Crack Growth Process Including Multiple Inspections

Figure 28.35 shows the corrosion-fatigue-crack growth process with and without crack detection inspections. The plots show the time evolution of the PDF of crack length in an axonometric view and, using contour right-side plots, this corresponds to four NDE inspections at 4000 flight hours (FH) each. After each inspection, new cracks are born due to the repair or replacement of components with large cracks. The new crack populations are introduced by the removal of large cracks in the previous crack populations. An accurate stochastic modeling of the corrosion-fatigue-crack growth process, including inspections, has to include the presence of multiple statistical crack size populations. A nonnormal probabilistic mixture model is used for the crack size populations. For each crack size population, a nonnormal probability distribution is assumed.

28.5 Illustrative Examples

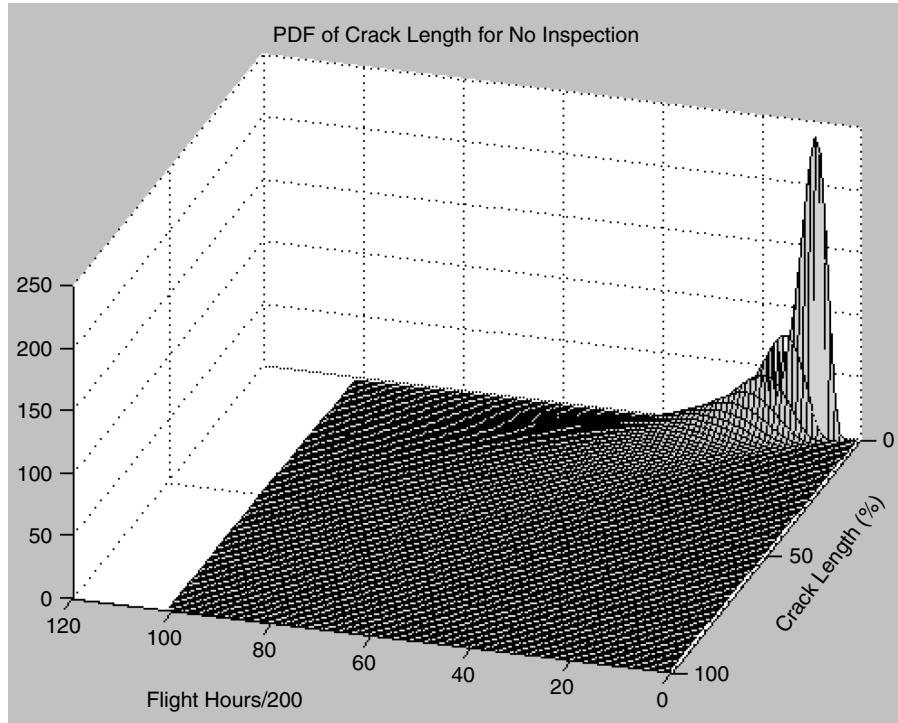
To keep the discussion simple, the illustrative examples presented in this section include only the effect of pitting corrosion on corrosion-fatigue life. The effects of other corrosion types, including intergranular corrosion in early stages or general thickness loss and pilling in later stages, are not considered. No cladding was assumed. Also, the multiple site damage (MSD) or widespread fatigue damage (WFD) that usually produces the ultimate lap-joint system failures are not included. Only the local failure in critical locations is considered. However, both MSD and WFD are real threats to aircraft structural integrity and therefore they must be considered when evaluating the risk of failure for an actual aircraft structure.

Several examples of probabilistic life prediction and risk-based maintenance analysis against corrosion-fatigue damage are shown in this section:

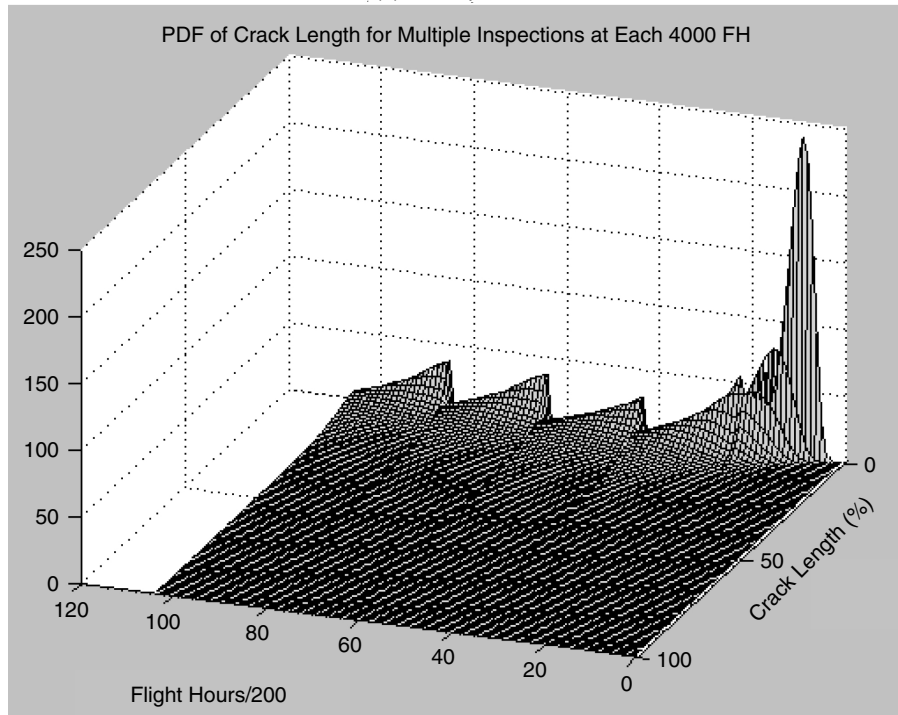
1. Probabilistic life predictions using the WCF, CCCF, and SCF models
2. Risk-based optimal cost analysis for a typical component
3. Risk-based maintenance analysis for a typical aircraft lap joint (Figure 28.1), including the effect of randomly rotating the aircraft to different airfields

28.5.1 Probabilistic Life Prediction Using Different Corrosion-Fatigue Models

In the first example, the CCCF model (using a modified FASTRAN version) is used to compute the corrosion-fatigue life of thin 2024-T3 aluminum sheets [44]. The surface constituent particle size was statistically modeled using a lognormal probability distribution based on the results of Laz and Hillberry [44]. The simulated PDF of the particle size is plotted in Figure 28.36. Figure 28.37 shows the computed probabilistic fatigue life and corrosion-fatigue life assuming airport locations with different environmental severities. Figure 28.38 shows the fatigue life vs. the corrosion-fatigue life for all the airport locations



(a) No Inspection



(b) Multiple Inspections at Each 4000 FH

FIGURE 28.35 Evolution of crack-length development: (a) no inspection; (b) multiple inspections at each 4000 flight hours.

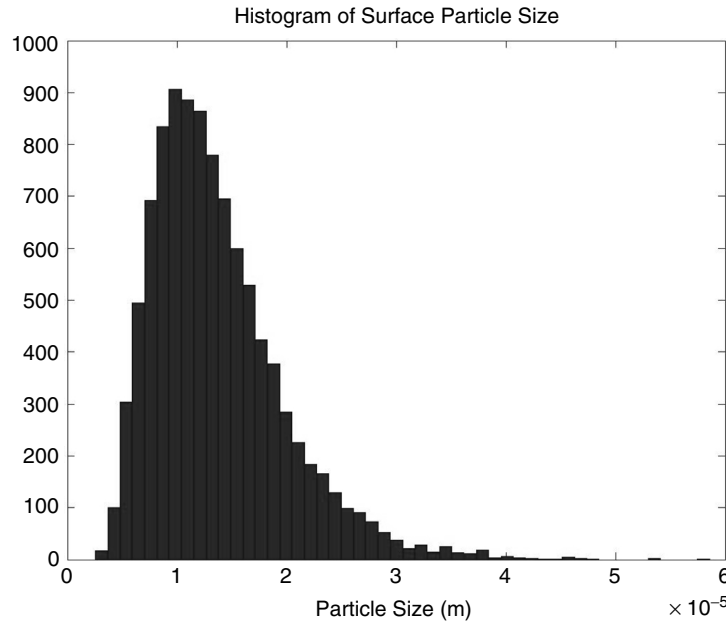
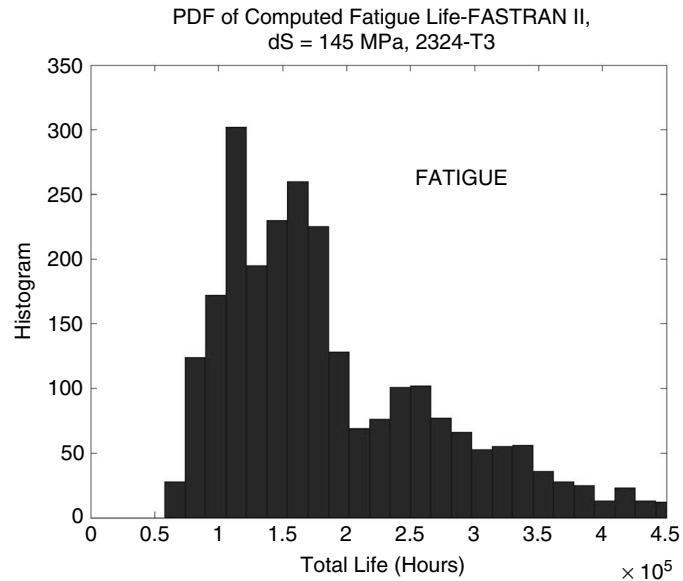


FIGURE 28.36 Simulated PDF of the surface constituent particle size.

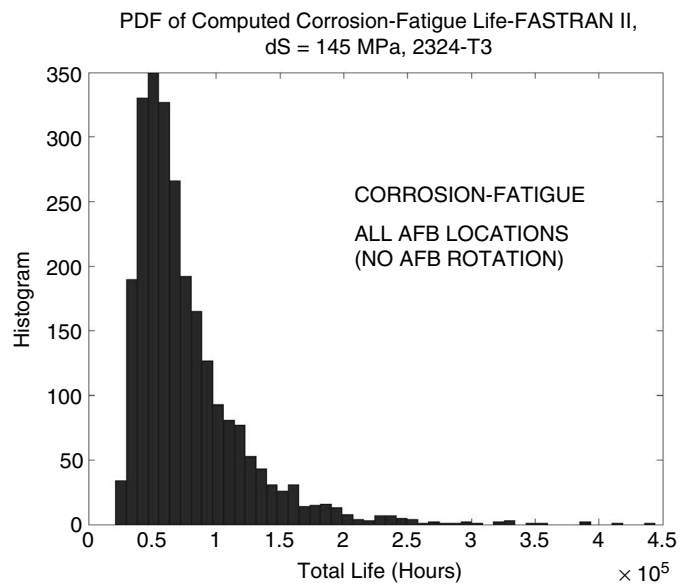
considered. It should be noted that the corrosion effects reduce the component fatigue life up to 10 to 15 times. Figure 28.39 shows the plot of the corrosion-fatigue life vs. the particle size. As shown, there is a relatively weak negative statistical correlation between corrosion-fatigue life and particle size. This indicates that particle size may not be a governing parameter for the corrosion-fatigue-life prediction (the random corrosion effects influence the life more significantly). This negative correlation is much stronger between pure fatigue life and particle size, as shown in Figure 28.40. Thus, for pure fatigue damage, the role of the particle size on the predicted life is significantly greater than for corrosion-fatigue damage.

The second example is a comparison between the WCF model and the SCF model for assessing the probabilistic corrosion-fatigue life of an aircraft component. The material considered is 2024-T3 aluminum. The constituent surface particle sizes, the threshold stress intensity range ΔK_{th} , and the pit depth were assumed to be random variables for the probabilistic life prediction. The constituent particle size distribution is lognormal based on the data of Laz and Hillberry [43, 44], as shown in Figure 28.36. The stress-intensity-range threshold was modeled by a normal variable with mean of $3 \text{ MPa}\sqrt{\text{m}}$ and a coefficient of variation of 0.10. The pit depth at any arbitrary time was modeled by a random scale factor between 1 and 21 applied to a mean $I_{p0} = 0.5 \text{ C/sec}$. The pit scale factor was introduced to simulate the different environmental severity conditions at various airport locations. The fatigue-crack-propagation models included in the WCF and SCF models are the truncated Paris-law crack-growth model and, respectively, the Forman crack-growth model. They are compared in Figure 28.41. From this figure it can be observed that for stress intensity ranges that only are slightly larger than the threshold of $3 \text{ MPa}\sqrt{\text{m}}$, the WCF model assumes much higher crack growth rates than the SCF model. This behavior is expected to reduce the fatigue life computed with the WCF model.

Figure 28.42 and Figure 28.43 show the probabilistic corrosion-fatigue life computed for the two aircraft operating scenarios of two load cycles/day and ten load cycles/day, respectively, assuming that the mean duration of one cycle (flight) is 1.5 hours. The probabilistic life estimations indicate that the WCF model overestimates the statistical variability of the corrosion-fatigue life due to two modeling



(a) Pure Fatigue



(b) Corrosion-Fatigue Including Different Airport locations

FIGURE 28.37 Predicted-life PDF computed using CCCF model: (a) pure fatigue; (b) corrosion fatigue including different airport locations.

effects: (1) it exaggerates the crack growth rates for ΔK slightly above ΔK_{th} , so that it produces a shorter life of some components, and (2) it does not include the effect of pitting on crack growth, so that it produces a longer life of some other components. The first effect, item 1, is stronger and more visible when the fatigue damage is greater, i.e., greater for ten cycles/day than for two cycles/day. The second effect, item two, is more visible when the *corrosion* damage is greater, i.e., greater for two cycles/day than for ten cycles/day.

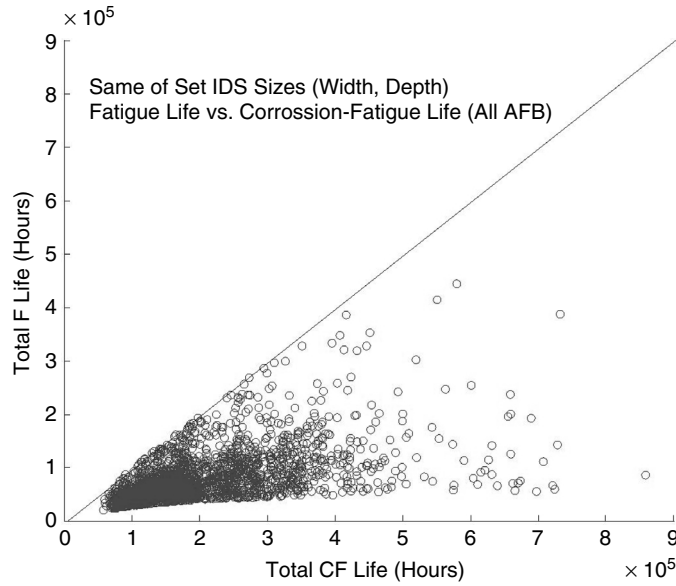


FIGURE 28.38 Fatigue life vs. corrossion-fatigue life.

28.5.2 Risk-Based Maintenance Analysis of a Lap Joint Subjected to Pitting Corrosion and Fatigue

The reliability analysis was performed for the aircraft lap joint shown in Figure 28.1. The major loading in the lap joint comes from the pressurization in the aircraft. Figure 28.44 shows the load transfer with the aircraft lap-joint components. The input random variables included in the reliability analysis are shown in Table 28.9.

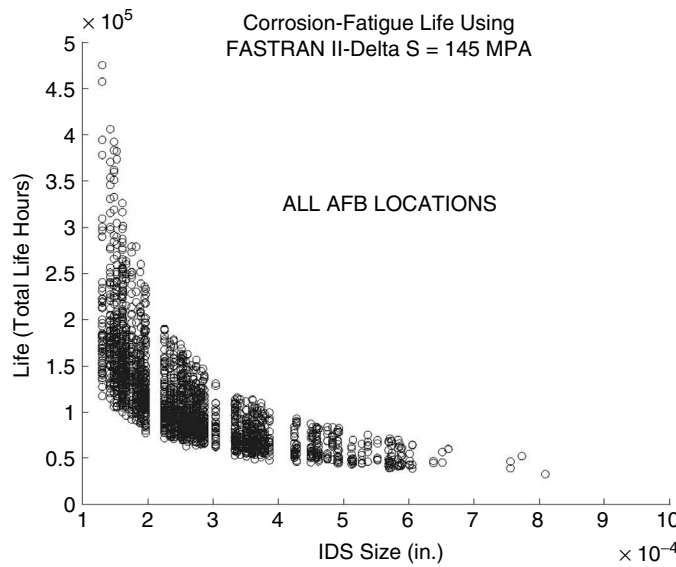


FIGURE 28.39 Corrossion-fatigue life vs. surface particle size.

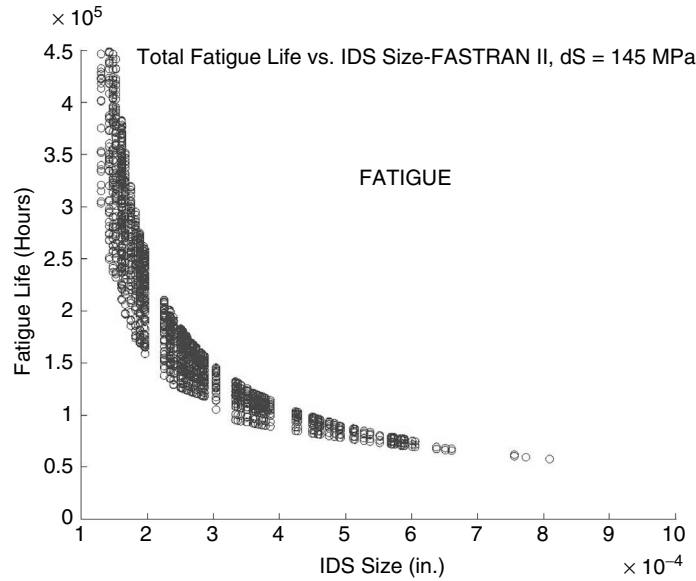


FIGURE 28.40 Pure fatigue life vs. surface particle size.

Figure 28.45 illustrates the stochastic history of pressure loading and environmental conditions of the aircraft. The elementary constituent of the stochastic history of the lap joint is the block that includes a single flight and a single stay on ground. It was assumed that the random pressure load is described by a single cycle for each flight. The environmental severity condition that drives corrosion was considered to randomly vary with the airport location. However, for the same location it was assumed that the environmental condition is a time-invariant quantity.

Figure 28.46 illustrates the simulated PDF of the pit growth volumetric rate based on the assumption shown in Table 28.9. The surface particles were assumed to be the initiators of the pits and microcracks.

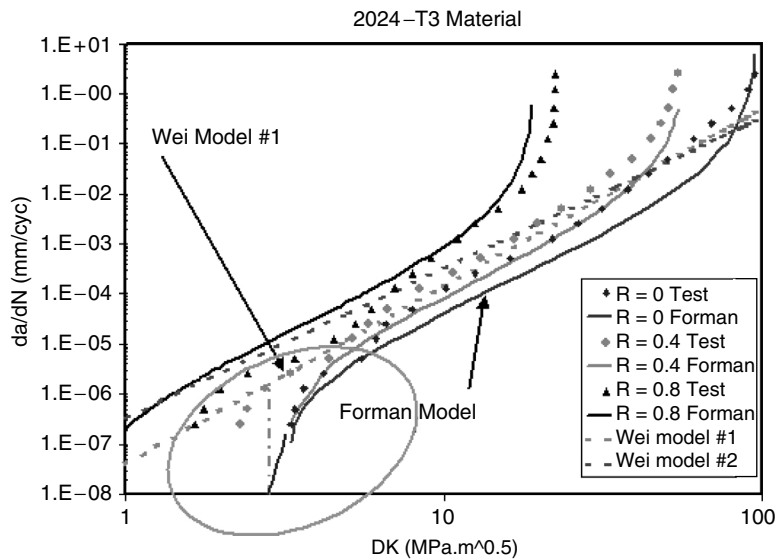


FIGURE 28.41 Comparison of fatigue-cracking models.

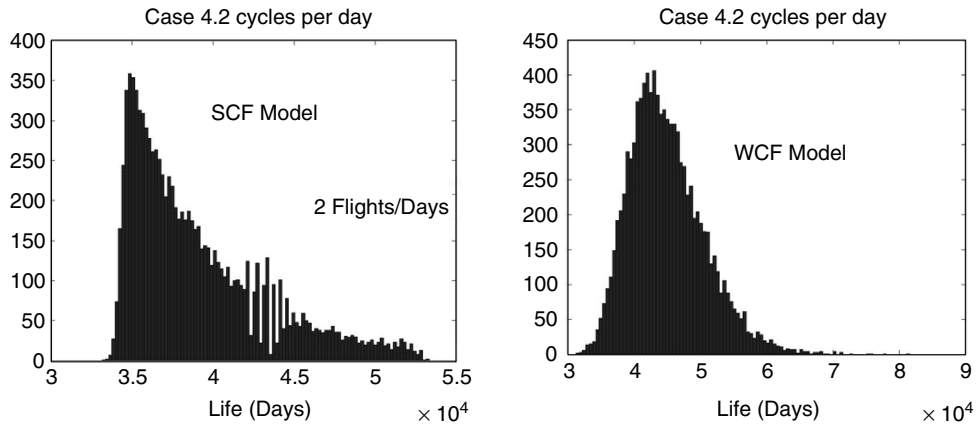


FIGURE 28.42 PDF of predicted life for the SCF and WCF models for 2 cycles/day.

From Figure 28.46, it should be noted that the environmental severity condition characterized by pit growth rate has a highly skewed probability distribution. Figure 28.46 indicates that the environmental severity conditions expressed by the pit growth rates are mild for most of the airport locations and severe for only a few locations. A truncated exponential distribution was used to fit the trend of the measured corrosion rate data at different airport locations [8, 60]. These large differences in values indicate that the crevice pits can grow up to ten times faster in some airport locations than in others.

Four flight scenarios were investigated for reliability analysis of the aircraft lap joint. The four scenarios were obtained by combining two aircraft operating scenarios with two flying scenarios. The two operating scenarios were (a) one flight/day and (b) three flights/day, and each of these was applied in two flying scenarios: (1) each aircraft flies from an airport location to the same airport location, without random rotation of the airport location, and (2) each aircraft flies randomly from an airport location to any other airport location, with random rotation of the airport location. In the last flying scenario, it was assumed that all airport locations are equally probable and that each individual aircraft can visit all airport locations. This is the ideal situation for reducing scatter of the corrosion effect, assuming a uniform distribution of the aircraft fleet across the airport location set.

To compute the probabilistic corrosion-fatigue life of the lap joint, both the crack-initiation and the crack-propagation stages were included. The stochastic strain-life curve and the stochastic Forman

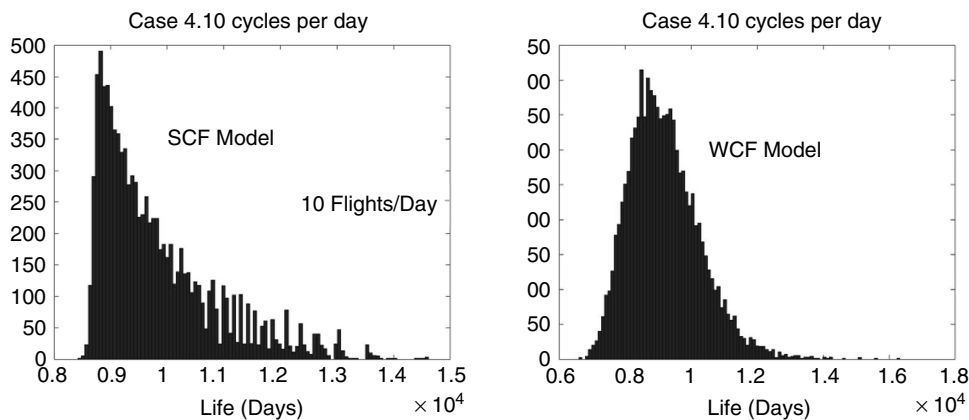


FIGURE 28.43 PDF of predicted life for the SCF and WCF models for 10 cycles/day.

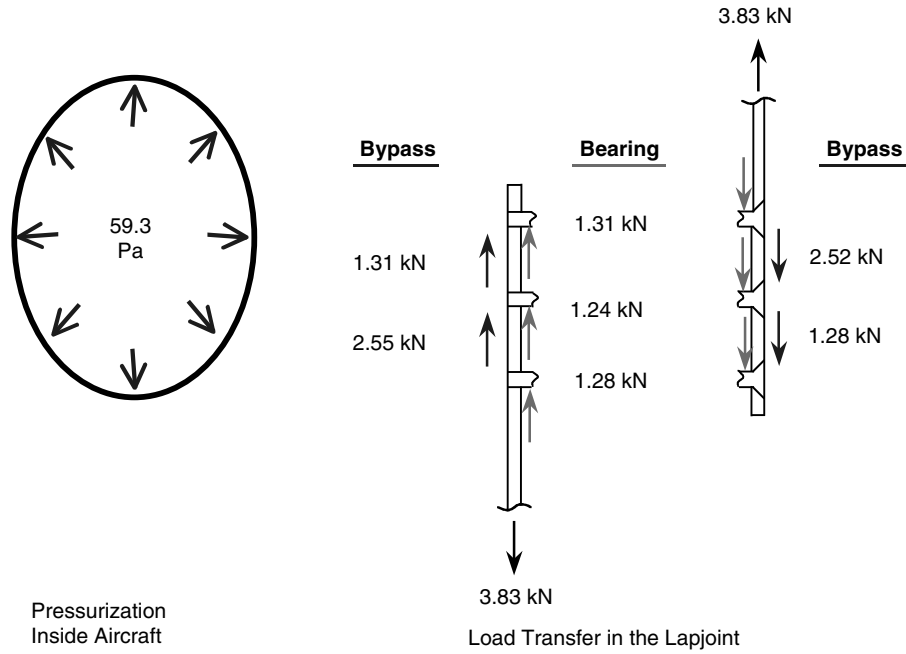


FIGURE 28.44 Pressure load transfer in the lap-joint components — fasteners and splices.

TABLE 28.9 Input Random Variables Included in the Reliability Analysis

Random Parameter	Mean	Standard Deviation	Probability Distribution
Uniform pressure inside aircraft, p (Pa)	59.3	2.97	normal
Single flight duration, d (h)	2.8	0.50	lognormal
Surface particle size, a_0 (μm)	13.66	6.02	Weibull (Figure 28.36)
Strain life curve exponents, b and c	-0.114, -0.927	0.00114, 0.00927	normal, normal
Strain life curve parameters, σ'_f (MPa) and ϵ'_f	1044	20.88	normal
	1.765	0.0353	normal
Stress-intensity-range threshold, ΔK_{th} (MPa $\sqrt{\text{m}}$)	3.00	0.15	normal
Toughness, K_c (MPa $\sqrt{\text{m}}$)	97.7	2.93	normal
Pit-growth parameter, I_{PO} , in Wei model variation due to different environmental conditions for different airport locations (C/sec)	14.08	22.26	truncated exponential 0.1–100 C/sec(Figure 28.46)

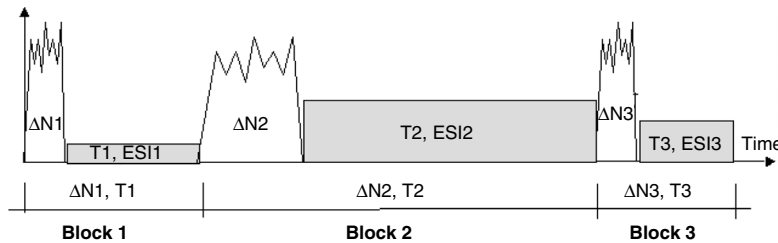


FIGURE 28.45 Stochastic history of loading and environmental conditions.

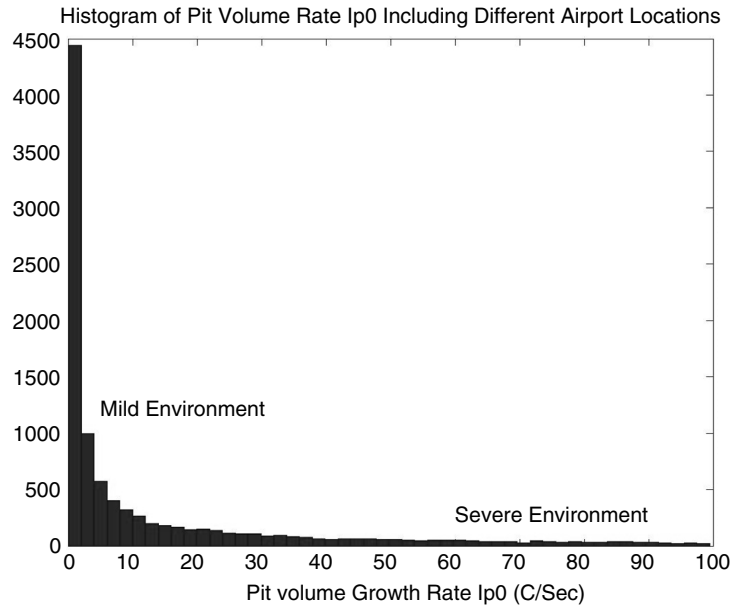


FIGURE 28.46 Simulated PDF of the pit-growth volumetric rate.

crack-propagation models were developed from the deterministic models based on the assumption that their parameters are random quantities, as shown in Table 28.9. To include the effect of pitting corrosion on the lap-joint fatigue life, a SCF model was employed.

Figure 28.47 and Figure 28.48 show the simulated pit depth growth curves for all airport locations assuming no rotation of airport locations. These pit curves were computed using Wei pitting model

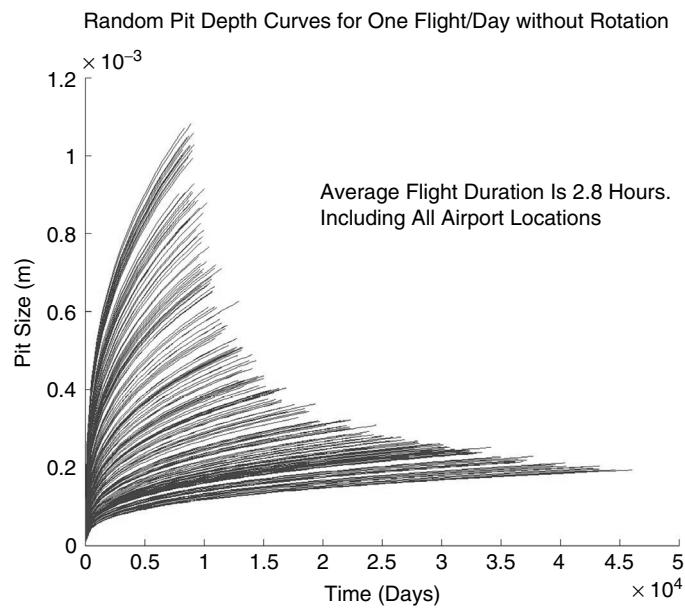


FIGURE 28.47 Simulated pit-growth curves for one flight/day without airport rotation.

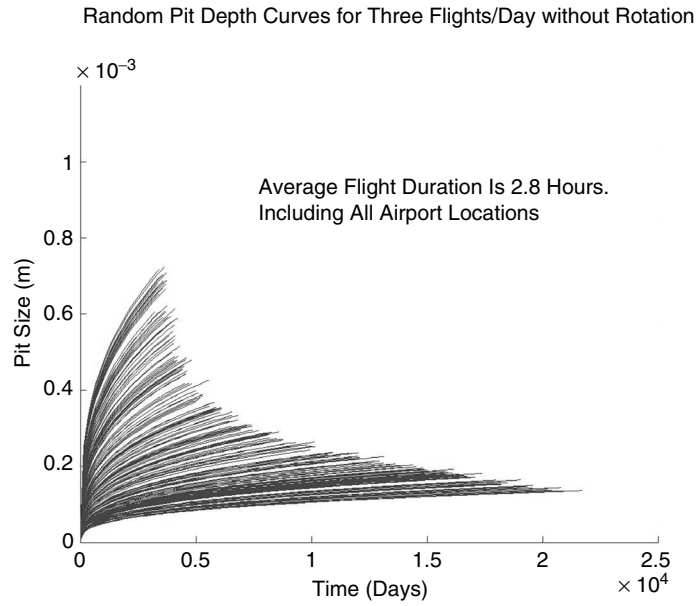


FIGURE 28.48 Simulated pit-growth curves for three flights/day without airport rotation.

(Equation 28.20). The pit growth curves shown in the figures stop at the failure times. Figure 28.47 is for the one-flight/day scenario and Figure 28.48 is for the three-flights/day scenario, respectively. Figure 28.49 and Figure 28.50 show the pit-growth curves for the same two scenarios with a random rotation of aircraft location. It was assumed that each aircraft has an equal probability to fly to any airport location. This means there is a high probability that each airport will be visited about the same number of times by each aircraft. Therefore, for the scenario with the airport rotation, the scatter of the pit growth

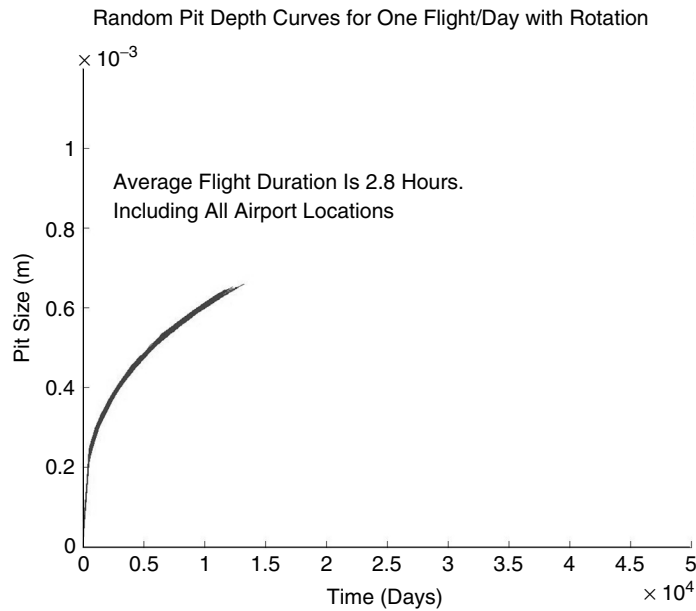


FIGURE 28.49 Simulated pit-growth curves for one flight/day with airport rotation.

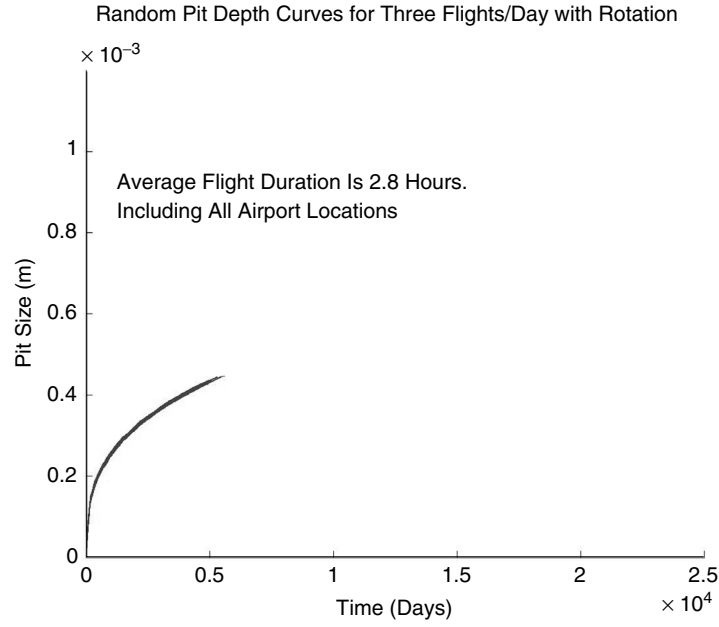


FIGURE 28.50 Simulated pit-growth curves for three flights/day with airport rotation.

drops significantly, converging in the limit to the (deterministic) mean pit growth for an infinite number of flights per aircraft.

The simulated crack-length curves are plotted in Figure 28.51 through Figure 28.54 for the four investigated scenarios. The computed histograms (with different incremental steps) of predicted corrosion-fatigue life of the four cases are shown in Figure 28.55. It should be noted that the mean

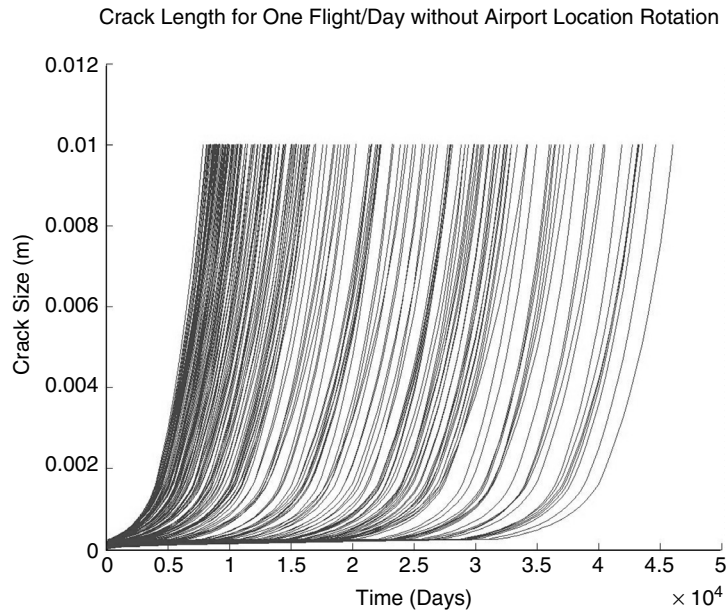


FIGURE 28.51 Simulated crack-size curves for one flight/day without airport rotation.

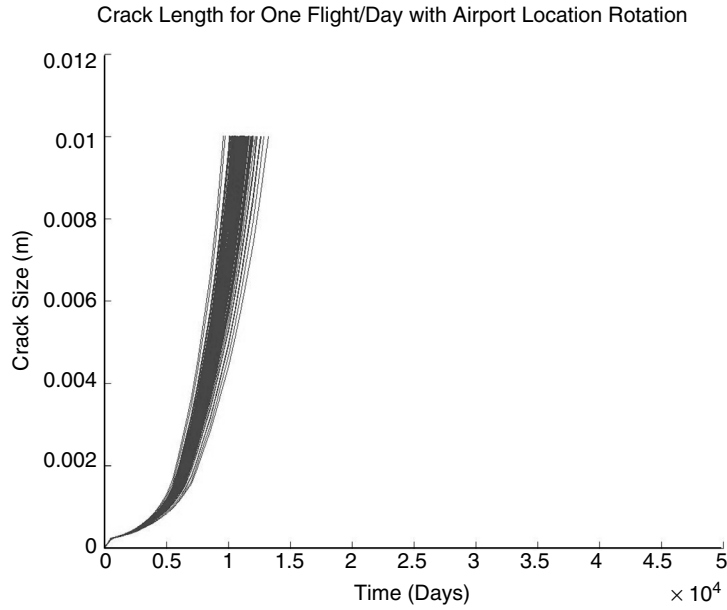


FIGURE 28.52 Simulated crack-size curves for one flight/day with airport rotation.

corrosion-fatigue life is about double for the one-flight/day scenario vs. three-flights/day scenario. Figure 28.56 and Figure 28.57 illustrate the probability density of the time until a 5.0-mm crack length is reached for the one-flight/day scenario, without airport rotation and with airport rotation, respectively. The computed probability densities (PDF) are compared with analytical densities, namely the lognormal and normal probability densities. It should be noted that for the case without rotation, the computed skewed density is far from the lognormal density, while for the case with rotation, the

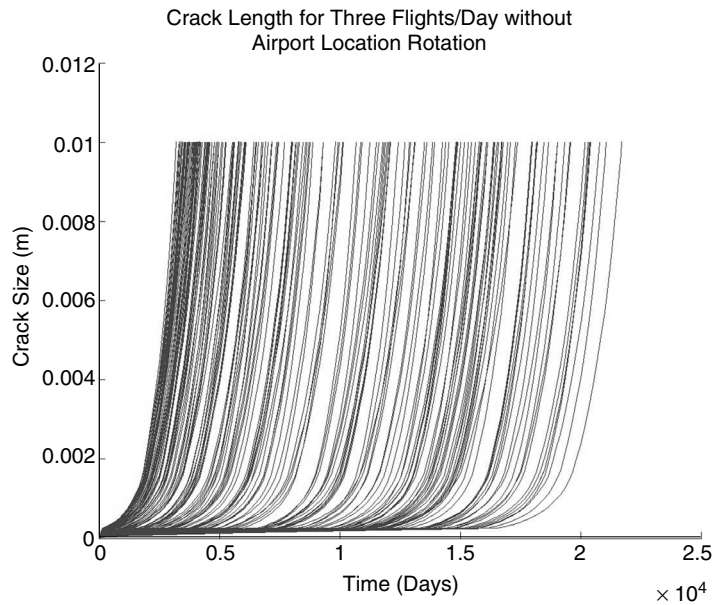


FIGURE 28.53 Simulated crack-size curves for three flights/day without airport rotation.

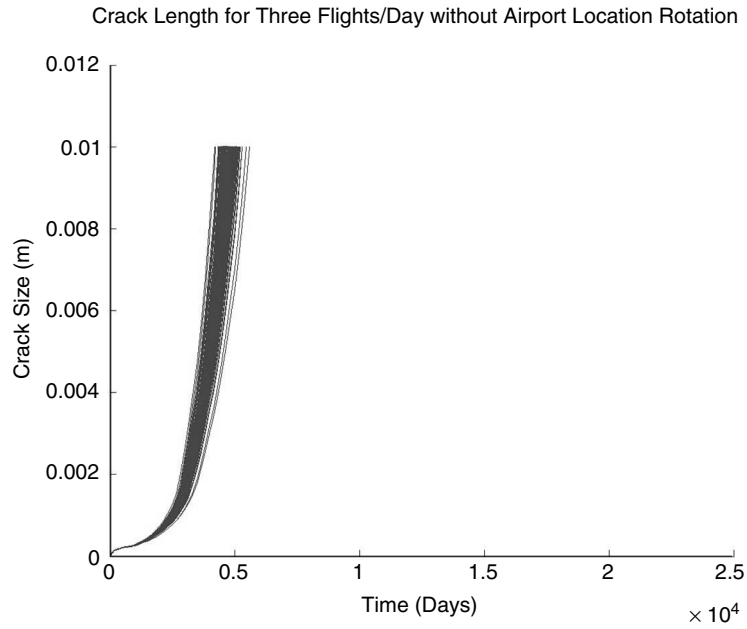


FIGURE 28.54 Simulated crack-size curves for three flights/day with airport rotation.

computed density is very close to normal density. For the former case, without rotation, the heavy right tail of the PDF shape is due to the fact that many airport locations have milder environmental-severity conditions, as indicated in Figure 28.46. For the latter case, the scatter of corrosion effects is reduced and the predicted-life probability density converges to the normal distribution in accordance with the central limit theorem.

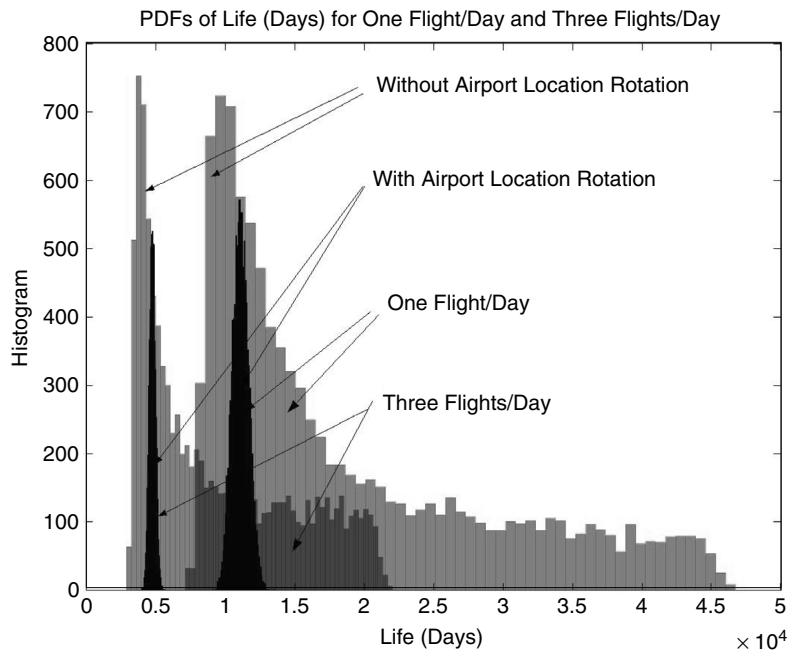


FIGURE 28.55 Corrosion-fatigue histograms (different steps) for the investigated scenarios.

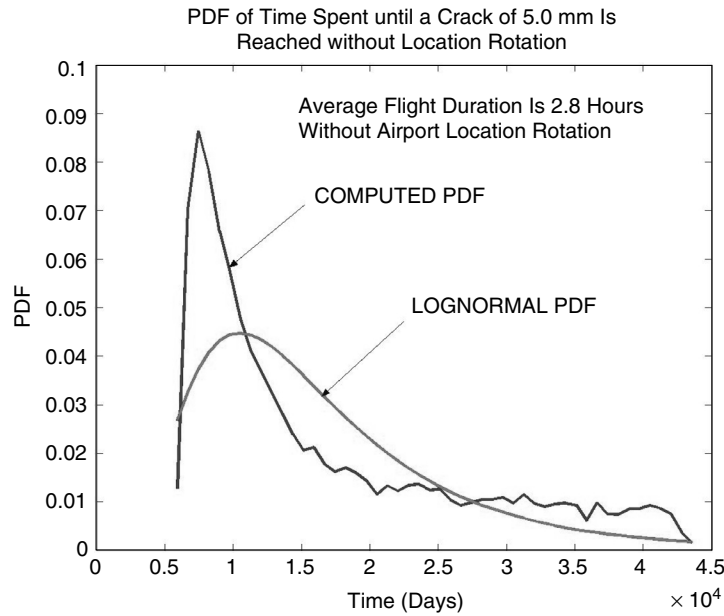


FIGURE 28.56 PDF of corrosion-fatigue life for one flight/day without airport rotation.

To consider the effect of maintenance, the uncertainties associated with the probability of crack detection for different standard NDE inspections were included using the appropriate POD curves. The eddy-current NDE technique with different operator skill classes was considered. The eddy-current POD curve was assumed to correspond to a lognormal distribution with a logarithmic mean and logarithmic standard deviation of (a) -4.73 and 0.98 for the best operator, (b) -3.75 and 0.70 for the average operator, and (c) -2.73 and 0.45 for the worst operator. No crack sizing error was included in addition to operator's

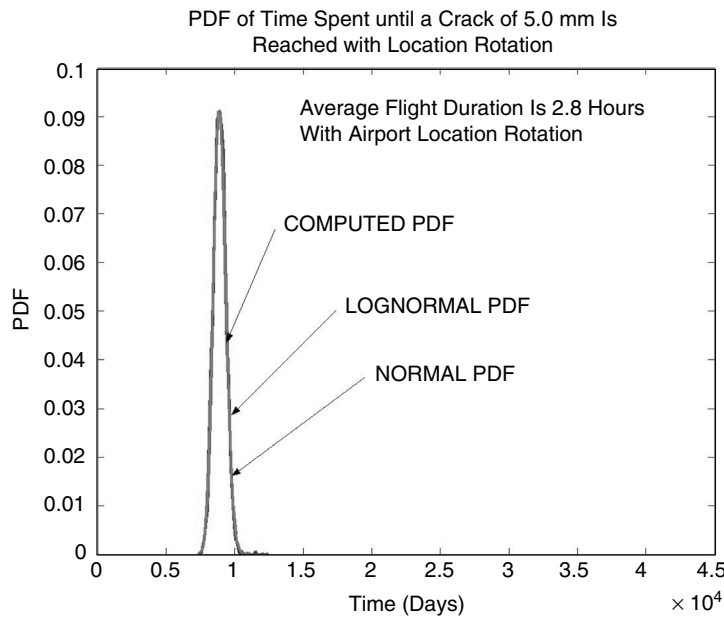


FIGURE 28.57 PDF of corrosion-fatigue life for one flight/day with airport rotation.

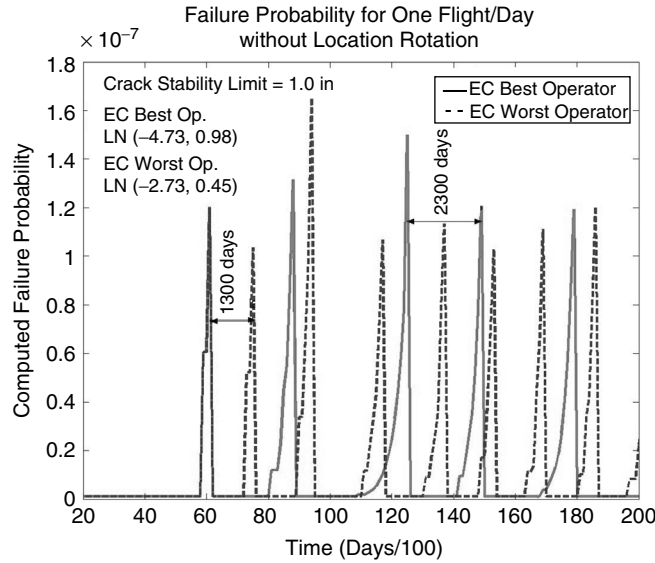


FIGURE 28.58 Risk-based inspection times for one flight/day, without rotation, for a given target risk of 2×10^{-7} : effect of the operator's skill.

skill variation. At each inspection time, the statistical crack population was filtered through the POD curve. Based on the computed probabilities of acceptance or rejection, each crack was randomly accepted or removed by replacing the cracked component. The repair effects were not considered for this illustrative example.

Figure 28.58 through Figure 28.61 indicate the inspection schedule required over 20,000 days (about 60 years) for maintaining the corrosion-fatigue damage risk under a reliability target defined by an upper-bound failure probability of 2×10^{-7} . Figure 28.58 and Figure 28.59 show the results computed for the

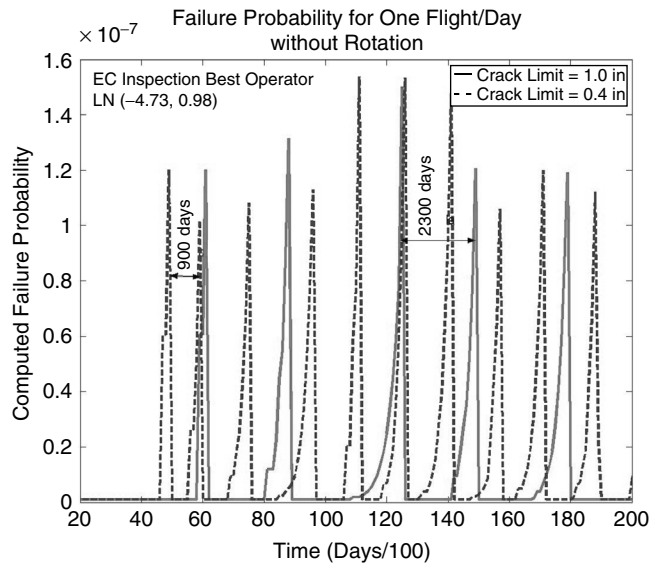


FIGURE 28.59 Risk-based inspection times for one flight/day, without rotation, for a given target risk of 2×10^{-7} : effect of crack-limit criterion.

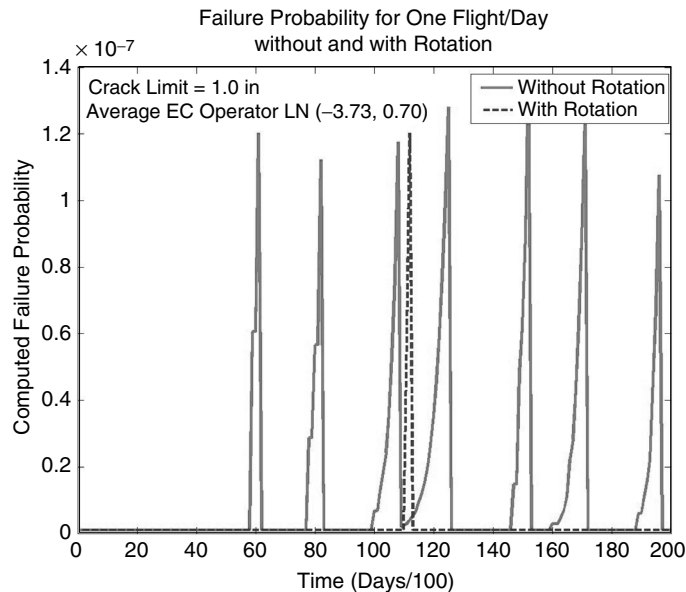


FIGURE 28.60 Risk-based inspection times for one flight/day without and with rotation.

one-flight/day scenario without airport rotation. Figure 28.58 compares results for different NDE operator's skills (best operator vs. worst operator), while Figure 28.59 compares results for different failure limit criteria (crack limit of 1.0 in. vs. crack limit of 0.40 in.). It should be noted that the minimum inspection interval drops from 2300 days (6450 flight hours [FH]) to 1300 days (3640 FH) due to the NDE operator's skill, and from 2300 days (6540 FH) to 900 days (2520 FH) due to the crack-limit criterion considered.

Figure 28.60 and Figure 28.61 compare the required inspection schedules for the two cases, without and with airport rotation, including both the one-flight/day scenario and three-flights/day scenario, assuming the same reliability target, an average operator's skill, and a 1.0-in. crack-limit failure criterion.

Without the airport rotation, the required inspection intervals in real time are about two or three times longer for the one-flight/day scenario than for the three-flights/day scenario. However, if the inspection intervals are measured in effective FH instead of days, this observation is not true. The minimum inspection intervals are 1600 days (4480 FH) for the one-flight/day scenario and 600 days (5040 FH) for the three-flights/day scenario. The increase of the inspection intervals expressed in flight hours from the one-flight/day scenario to three-flights/day scenario indicates that the effects of corrosion are more severe for one-flight/day when the time spent by an aircraft on ground is longer.

With the airport rotation, the minimum inspection intervals are much longer than those computed without airport location rotation. The minimum inspection intervals are 11,200 days (31,360 FH) for the one-flight/day scenario and 4,600 days (38,640 FH) for the three-flights/day scenario. This large benefit effect of the random rotation of airport locations is mainly a result of the large reduction in the statistical scatter of corrosion effects as a result of the central limit theorem.

The exclusive use of *instantaneous* failure probabilities to characterize aircraft reliability is insufficient for setting the risk-based maintenance strategy. This is because, from a risk-based-maintenance point of view, one is interested in the aircraft reliability over a period of time, not only at the critical instantaneous times. To illustrate the point, we can review the results in Figure 28.60. For the inspection schedule shown, the maximum risk is almost constant with a value of 1.2×10^{-7} . The maximum risk is bounded to 1.2×10^{-7} independent of the aircraft operating scenarios, without or with airport location rotation. However, the number of inspections is different, so that the number of times when the maximum failure

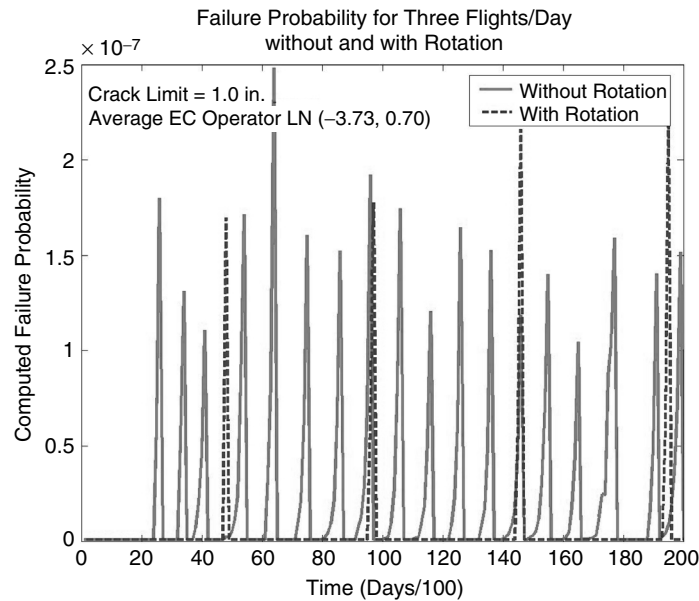


FIGURE 28.61 Risk-based inspection times for three flights/day without and with rotation.

risk is reached is different for the two operating scenarios. Thus, if the average hazard failure rates over a long period are computed, they are very different. For the results in Figure 28.60, if the average hazard failure rates are computed over the 20,000-day (about 60 years) period, these are 1.04×10^{-10} events/day and 7.97×10^{-12} for the cases without airport rotation and with rotation, respectively. This means that, in the long run, the average number of aircrafts having failures is about ten times higher for the case without airport rotation than the case with rotation, although the maximum instant risk is the same for the two cases. Thus, to maintain the same aircraft reliability for the two cases, it would be necessary to define different target instantaneous risks for the two cases, about an order of magnitude lower for the case without rotation, so that finally we end up with the same average hazard rates over the period of interest. Failure probabilities are good reliability metrics for time-invariant or instantaneous reliability problems, while average hazard failure rates are good reliability metrics for time-variant problems such as the risk-based maintenance problem.

The above discussion also indicates that the age distribution of the aircraft fleet plays an important role on the aircraft fleet reliability over a given period of time. Figure 28.60 shows that for different time periods, for example 7000 days (about 20 years), depending on the aircraft fleet age distribution and its variation in the selected periods, the individual aircraft risks can vary wildly. As a consequence of this, the average fleet hazard failure rates can vary about two orders of magnitude for different time periods and different fleet age distributions.

28.6 Concluding Remarks

This chapter presents an overview of the key engineering issues that are important for performing a reliability analysis of aircraft structure joints under corrosion-fatigue damage. The chapter focused on probabilistic modeling of stochastic cumulative damage due to corrosion fatigue. Different corrosion-fatigue models are reviewed in relative detail, and their results are compared. One model was then applied to the probabilistic life prediction and risk-based maintenance analysis of an aircraft fuselage lap joint. For this illustrative example, the loading stochasticity was limited to the small

variability of aircraft pressurization. Variability-related structural modeling and analysis, as well as the stochasticity of the loading and load transfer through the structure to the individual fasteners, was ignored in order to keep the example simple.

Computational risk-based maintenance using physics-based stochastic damage models, carefully calibrated with the appropriate empirical data, provides a quantitative process for simultaneously maximizing aircraft availability and reducing maintenance costs while maintaining safety and airworthiness. The physics-based stochastic modeling tools and computational reliability methods are sufficiently mature to approach the difficult problem of aircraft fleet maintenance from a probabilistic risk-based perspective.

An important practical aspect, not discussed herein, is that probabilistic models need to be implemented so that they can incorporate new information and statistical data coming from lab tests, depot maintenance, and service history. Refinement of the probabilistic models in this way will make risk predictions sharper by reducing their statistical confidence intervals (reducing uncertainties due to modeling and lack of data).

References

1. U.S. Air Force, Aircraft Structural Integrity, AFD 63-10, US Air Force Publications Distribution Center, Baltimore, 1997. (also www.e-publishing.af.mil)
2. U.S. Air Force, Aircraft Structural Integrity Program, AFI 63-1001, U.S. Air Force Publications Distribution Center, Baltimore, 2002. (also www.e-publishing.af.mil)
3. U.S. Air Force, *General Guidelines for Aircraft Structural Integrity Program*, MIL-STD-1530B, Aeronautical Systems Center, Wright-Patterson Air Force Base, OH, 2004. (also www.dodssp.daps.mil)
4. Damage Tolerance and Fatigue Evaluation of Structure, Federal Aviation Regulation, Part 25, Airworthiness Standards: Transport Category Airplanes, Sec. 25.571.
5. Damage Tolerance and Fatigue Evaluation of Structure, Joint Aviation Requirements, Part 25 Large Aeroplanes, Section 25.571. (available at <http://www.jaa.nl>)
6. Protection of Structure, Federal Aviation Regulation, Part 25, Airworthiness Standards: Transport Category Airplanes, Sec. 25.609.
7. Protection of Structure, Joint Aviation Requirement, Part 25, Large Aeroplanes, Section 25. 609. (available at <http://www.jaa.nl>)
8. Brooks, C.L., "ECLIPSE-Environmental & Cyclic Life Interaction Prediction Software," Aeromat 1999, Dayton, OH. (available at http://www.apesolutions.com/firm_link.htm)
9. Gallagher, J.P., Giessler, F.J., Berens, A.P., and Engle, R.M. Jr., *USAF Damage Tolerant Design Handbook: Guidelines for the Analysis and Design of Damage Tolerant Aircraft Structure*, AFWAL-TR-82-3073 (ADA153161), Defense Technical Information Center, Ft. Belvoir, VA, May 1984, p. 1.4.3.
10. Rummel, W.D., and Matzkanin, G.A., *Nondestructive Evaluation (NDE) Capabilities Databook*, ADA286978, 3rd Ed., Defense Technical Information Center, Ft. Belvoir, VA, 1997.
11. Yee, B.G.W., Chang, F.H., Couchman, J.C., Lemon, G.H., and Packman, P.F., *Assessment of NDE Reliability Data*, NASA-CR-134991 (ADA321309), Defense Technical Information Center, Ft. Belvoir, VA, 1974.
12. Matzkanin, G.A., and Yolken, H.T., *A Technology Assessment of Probability of Detection (POD) for Nondestructive Evaluation (NDE)*, NTIAC-TA-00-01 (ADA398282), 2001.
13. Hoppe, W., Pierce, J. and Scott, O., *Automated Corrosion Detection Program*, AFRL-ML-WP-TR-2001-4162 (ADA406600), Defense Technical Information Center, Ft. Belvoir, VA, 2001.
14. U.S. Dept. of Defense, Joint Service Specification Guide: Aircraft Structures, JSSG-2006, Appendix A.3.1.2, Requirement Guidance, Dept. of Defense, Washington, D.C., 1998. (also www.dodssp.daps.mil)
15. Lincoln, J.W., Risk assessments of aging aircraft, in *Proc. 1st Joint DoD/FAA/NASA Conf. on Aging Aircraft*, Vol. 1, Air Force Wright Aeronautics Laboratory, Wright-Patterson Air Force Base, OH, 1997, pp. 141-162.

16. Berens, A.P., Hovey, P.W., and Skinn, D.A., *Risk Analysis for Aging Aircraft Fleets*, Vol. 1, *Analysis*, WL-TR-91-3066 (ADA252000), Defense Technical Information Center, Ft. Belvoir, VA, 1991.
17. Hovey, P.W., Berens, A.P., and Loomis, J.S., *Update of the Probability of Fracture (PROF) Computer Program for Aging Aircraft Risk Analysis*, Vol. 1, *Modifications and User's Guide*, AFRL-VA-WP-TR-1999-3030 (ADA363010), Defense Technical Information Center, Ft. Belvoir, VA, 1998.
18. Broeck, David, Residual strength of metal structures, in *ASM Handbook*, Vol. 19, *Fatigue and Fracture*, Lampman, S.R., Ed., ASM International, Materials Park, OH, 1996, pp. 427–433.
19. U.S. Air Force, *Metallic Materials and Elements for Aerospace Vehicle Structures*, Mil-Hdbk-5H, Defense Area Printing Service, Philadelphia, 2001. (also www.dodssp.daps.mil)
20. Skinn, D.A., Gallagher, J.P., Berens, A.P., Huber, P.D., and Smith, J., *Damage Tolerant Design Handbook: a Compilation of Fracture and Crack Growth Data for High Strength Alloys*, Vol. 3, WL-TR-94-4054 (ADA311690), Defense Technical Information Center, Ft. Belvoir, VA, 1994.
21. Mishnaevsky, L.L., Jr., and Schmauder, S., Damage evolution and heterogeneity of materials: model based on fuzzy set theory, *Eng. Fracture Mechanics*, 57(6), 625–636, 1997.
22. Moller, B., Graf, W. and Beer, M., Safety assessment of structures in view of fuzzy randomness, *Comput. Struct.*, 81, 1567–1582, 2003.
23. Mitchell, M.R., Fundamentals of modern fatigue analysis for design, in *ASM Handbook*, Vol. 19, *Fatigue and Fracture*, Lampman, S.R., Ed., ASM International, Materials Park, OH, 1996, pp. 227–249.
24. Socie, D.F., and Morrow, JoDean, Review of contemporary approaches to fatigue damage analysis, *Risk and Failure Analysis for Improved Performance and Reliability*, Burke, J.J. and Weiss, V., Eds., Plenum Publishing Corp., New York, 1980, pp. 141–194.
25. Dowling, N.E., Estimating fatigue life, in *ASM Handbook*, Vol. 19, *Fatigue and Fracture*, Lampman, S.R., Ed., ASM International, Materials Park, OH, 1996, pp. 250–262.
26. Socie, D.F., Dowling, N.E., and Kurath, P., Fatigue life estimation of notched members, in *Fracture Mechanics: Fifteenth Symposium*, ASTM STP 833, Sanford, R.J., Ed., ASTM, Philadelphia, 1984, pp. 284–299.
27. Bucci, R.J., Nordmark, G., and Starke, E.A., Jr., Selecting aluminum alloys to resist failure by fracture mechanisms, in *ASM Handbook*, Vol. 19, *Fatigue and Fracture*, Lampman, S.R., Ed., ASM International, Materials Park, OH, 1996, pp. 771–812.
28. Peterson, R.E., *Stress Concentration Factors*, John Wiley & Sons, New York, 1974.
29. Bannantine, J.A., Comer, J.J. and Handrock, *Fundamentals of Metal Fatigue Analysis*, Prentice Hall, Englewood Cliffs, NJ, 1990.
30. Halford, G.A., Cumulative fatigue damage modeling — crack nucleation and early growth, *Int. J. Fatigue*, 19(93), 253–260, 1997.
31. Lankford, J., The growth of small fatigue cracks in 7075-T6 aluminum, *Fatigue Eng. Mater. Struct.*, 5(3), 233–248, 1982.
32. Newman, J.C., Jr., and Edwards, P.R., *Short-Crack Growth Behaviour in an Aluminum Alloy — An AGARD Cooperative Test Programme*, AGARD R-732, National Technical Information Service (NTIS), Springfield, VA, 1988.
33. Edwards, P.R., and Newman, J.C., Jr., *Short-Crack Growth Behaviour in Various Aircraft Materials*, AGARD R-767, National Technical Information Service (NTIS), Springfield, VA, 1990.
34. Goto, M., Statistical investigation of the behaviour of small cracks and fatigue life in carbon steels with different ferrite grain sizes, *Fatigue Eng. Mater. Struct.*, 17(6), 635–649, 1994.
35. Pearson, S., Initiation of fatigue cracks in commercial aluminum alloys and the subsequent propagation of very short cracks, *Eng. Fracture Mech.*, 7, 235–247, 1975.
36. Kung, C.Y., and Fine, M.E., Fatigue crack initiation and microcrack growth in 2024-T4 and 2124-T4 aluminum alloys, *Metallurgical Trans. A*, 10A, 603–610, 1979.
37. Sigler, D., Montpettit, M.C., and Haworth, W.L., Metallography of fatigue crack initiation in overaged high-strength aluminum alloy, *Metallurgical Trans. A*, 14A, 931–938, 1983.

38. Li, P., Marchand, N.J., and Ilschner, B., Crack initiation mechanisms in low cycle fatigue of aluminum alloy 7075-T6, *Mater. Sci. Eng.*, A119, 41–50, 1989.
39. Butler, J.P., and Rees, D.A., Development of Statistical Fatigue Failure Characteristics of 0.125-inch 2024-T3 Aluminum Under Simulated Flight-by-Flight Loading, AFML-TR-74-124 (ADA002310), Defense Technical Information Center, Ft. Belvoir, VA, 1974.
40. Moore, N., Ebbeler, D. H., Newlin, L.E., Surtharshana, S., and Creager, M., “An Improved Approach for Flight Readiness Certification – Probabilistic Models for Flaw Propagation and Turbine Blade Fatigue Failure, Volume 1”, NASA-CR-194496, Dec. 1992.
41. Vanstone, R.H., Gooder, O.C. and Krueger, D.D., Advanced Cumulative Damage Modeling, AFWAL-TR-88-4146 (ADA218555), Defense Technical Information Center, Ft. Belvoir, VA, 1988.
42. Newman, J.C., FASTRAN-II, A Fatigue Crack Growth Structural Analysis Program, NASA TM-104159, National Aeronautics and Space Administration, Langley, VA, 1992.
43. Laz, P.J. and Hillberry, B.M., The Role of Inclusions in Fatigue Crack Formation in Aluminum 2024-T3, presented at Fatigue 96: 6th International Fatigue Congress, Berlin, Germany, 1996.
44. Laz, P.J. and Hillberry, B.M., Fatigue life prediction from inclusion initiated cracks, *Int. J. Fatigue*, 20(4), 263–270, 1998.
45. Virkler, D. A., Hillberry, B.M., and Goel, P.K., The Statistical Nature of Fatigue Crack Propagation, AFFDL-TR-78-43 (ADA056912), Defense Technical Information Center, Ft. Belvoir, VA, 1978.
46. Liao, M. and Xiong, Y., A risk analysis of fuselage splices containing multi-site damage and corrosion, presented at *41st Structures, Structural Dynamics, and Materials Conference*, AIAA-2000-1444, American Institute for Aeronautics and Astronautics, Reston, VA, 2000.
47. Hollingsworth, E.H., and Hunsicker, H.Y., Corrosion of aluminum and aluminum alloys, in *ASM Handbook*, Vol. 13, *Corrosion*, ASM International, Materials Park, OH, 1987, pp. 583–608.
48. Cole, G.K., Clark, G., and Sharp, P.K., The Implications of Corrosion with respect to Aircraft Structural Integrity, DSTO-RR-0102, DSTO Aeronautical and Maritime Research Laboratory, Melbourne, Australia, 1997.
49. Bell, R.P., Huang, J.T. and Shelton, D., Corrosion Fatigue Structural Demonstration Program, final report, Defense Technical Information Center, Ft. Belvoir, VA, to be published.
50. Szklarska-Smialowska, Z., Pitting corrosion of aluminum, *Corr. Sci.*, 41, 1743–1767, 1999.
51. Harlow, D.G. and Wei, R.P. Probability approach for prediction of corrosion and corrosion fatigue life, *AIAA J.*, 32(10), 2073–2079, 1994.
52. Wei, R.P., Corrosion and Corrosion Fatigue of Airframe Materials, DOT/FAA/AR-00/22, National Technical Information Service, Springfield, VA, 2000.
53. Brandt, S.M. and Adam, L.H., Atmospheric exposure of light metals, in *Metal Corrosion in the Atmosphere*, ASTM STP 435, ASTM, Philadelphia, PA, 1968, pp. 95–128.
54. Ailor, W.H., Jr., Performance of aluminum alloys at other test sites, in *Metal Corrosion in the Atmosphere*, ASTM STP 435, ASTM, Philadelphia, PA, 1968, pp. 285–307.
55. Sankaran, K.K., Perez, R., and Jata, K.V., Effects of pitting corrosion on the fatigue behavior of aluminum alloy 7075-T6: modeling and experimental studies, *Mater. Sci. Eng.*, A297, 223–229, 2001.
56. Zamber, J.E. and Hillberry, B.M., Probabilistic approach to predicting fatigue lives of corroded 2024-T3, *AIAA J.*, 37(10), 1311–1317, 1999.
57. Burynski, R.M., Jr., Chen, G.-S., and Wei, R.P., Evolution of pitting corrosion in a 2024-T3 aluminum alloy, in *Structural Integrity in Aging Aircraft*, AD-Vol. 47, ASME, New York, 1995, pp. 175–183.
58. Ghiocel, D.M., Combining Stochastic Networks, Bayesian Inference and Dynamic Monte Carlo for Estimating Variation Bounds of HCF Risk Prediction, presented at the *7th National Turbine Engine High Cycle Fatigue Conference*, Monterey, CA, April 16–19, 2003.
59. Ghiocel, D.M., Refined Stochastic Field Models for Jet Engine Vibration and Fault Diagnostics, presented at *International Gas Turbine & Aeroengine Congress, 2000 TURBO EXPO*, Munich, Germany, May 8–11, 2000.

60. Kinzie, R. Jr., Corrosion Suppression: Managing Internal & External Aging Aircraft Exposures, presented at *6th Joint FAA/DoD/NASA Conf. on Aging Aircraft*, Aircraft Structures Session 1A, San Francisco, 2002.
61. Abernethy, R.B., *The New Weibull Handbook*, R.B. Abernethy, 1993.
62. Liao, M, Forsyth, D.S., Komorowski, J.P., Safizadeh, M., Liu, Z. and Bellinger, N., Risk Analysis of Corrosion Maintenance Actions in Aircraft Structures, presented at ICAF 2003, *Fatigue of Aeronautical Structures As An Engineering Challenge*, Lausanne, 2003.
63. Rocha, M.M., Time-Variant Structural Reliability Analysis with Particular Emphasis on the Effect of Fatigue Crack Propagation and Non-Destructive Inspection, report 32-94, University of Innsbruck, Institute of Engineering Mechanics, 1994.
64. Koul, A.K., Bellinger, N.C. and Gould, G., Damage-tolerance-based life prediction of aeroengine compressor discs: II — a probabilistic fracture mechanics approach, *Int. J. Fatigue*, 12(5), 388-396, 1990.
65. Berens, A.P. and P.W., Hovey, Evaluation of NDE Reliability Characterization, AFWAL-TR-81-4160 (ADA114467), Defense Technical Information Center, Ft. Belvoir, VA, 1981.

